

10.02 Interior Structure, Composition, and Mineralogy of the Terrestrial Planets

F. Sohl, DLR Institute of Planetary Research, Berlin, Germany

G. Schubert, University of California, Los Angeles, CA, USA

© 2007 Elsevier B.V. All rights reserved.

10.02.1	Introduction	28
10.02.2	Observational Methods	29
10.02.2.1	Geodesy	29
10.02.2.2	Rotation and Tides	30
10.02.2.3	Gravity and Topography	31
10.02.2.4	Magnetic Fields	32
10.02.2.5	Electromagnetics	32
10.02.2.6	Seismology	33
10.02.2.7	Surface Geology and Composition	34
10.02.2.8	Material Properties	34
10.02.3	Interior Structure and Composition	35
10.02.3.1	Two- and Three-Layer Structural Models	35
10.02.3.2	Multilayer Structural Models	36
10.02.3.2.1	Governing equations	36
10.02.3.2.2	Equation of state	37
10.02.3.2.3	Boundary conditions	39
10.02.3.2.4	Numerical solution	39
10.02.4	Earth as a Type Example of a Terrestrial Planet	40
10.02.4.1	General	40
10.02.4.2	Interior Structure	40
10.02.4.3	Composition	41
10.02.4.4	Mineralogy	41
10.02.5	The Moon	42
10.02.5.1	General	42
10.02.5.2	Interior Structure	42
10.02.5.3	Composition	43
10.02.5.4	Lunar Crust	43
10.02.5.5	Lunar Seismology and Mineralogy	44
10.02.6	Mercury	47
10.02.6.1	General	47
10.02.6.2	Interior Structure	48
10.02.6.3	Composition	49
10.02.6.4	Magnetic Field	49
10.02.6.5	Future Exploration	50
10.02.7	Mars	51
10.02.7.1	General	51
10.02.7.2	Interior Structure	51
10.02.7.3	Composition	54
10.02.7.4	Mineralogy	55
10.02.7.5	Martian Seismicity	57
10.02.8	Venus	57
10.02.8.1	General	58
10.02.8.2	Interior Structure	58

10.02.8.3	Composition	58
10.02.8.4	Tectonism	59
10.02.8.5	Dynamics	59
10.02.9	Summary and Outlook	60
References		61

10.02.1 Introduction

The inner planets Mercury, Venus, Earth, and Mars and terrestrial-type bodies like the Moon and some of the outer planet satellites are mainly composed of silicate rock and metals like iron. They are characterized by relatively small masses and radii, and large densities in comparison to the giant planets of the outer solar system. Measurements of rotation and gravitational and magnetic fields indicate that the interiors of these bodies, like the interior of the Earth, are chemically and rheologically layered and subdivided into iron-rich cores, silicate mantles, and rocky crusts derived from partial melting of the mantles. It is generally believed that the internal differentiation of the terrestrial planets and major satellites took place early in their histories only shortly after accretion from colliding planetesimals (Kleine *et al.*, 2002). Even the asteroid 4 Vesta, an accretional remnant left over from that period reveals a variegated surface with characteristic spectral features hinting at a strongly differentiated interior (Richter and Drake, 1996, 1997; Ghosh and McSween, Jr., 1998; Drake, 2001; Keil, 2002; Kleine *et al.*, 2002).

The investigation of planetary interiors is among the most important scientific objectives of interplanetary space missions. The internal structure and bulk composition of terrestrial planetary bodies provide important clues on the origin and early evolution of the solar system. Many large-scale planetary processes are controlled by the internal structure of these bodies. Surface geology and tectonic features are mainly affected by mechanisms that dominate the transport of internal heat from the interior to the surface. The existence of self-sustained and/or induced magnetic fields requires reservoirs of electrically conducting fluids at some depth, providing additional constraints on the present thermal state of these bodies. Since a fluid layer within a planetary body mechanically decouples the deep interior from its outer portion, the propagation of seismic waves and the way in which a planet or

satellite responds to tides is strongly affected by the physical state of its interior.

Models of the interior structure of a number of terrestrial-type planetary bodies are shown in **Figure 1**. These models are based on theoretical considerations which are strongly constrained by Earth-based and remote-sensing observations, *in situ* measurements, and laboratory studies. Interior structure models aim at calculating (1) the volumes and masses of major chemical reservoirs that contribute to the bulk composition; (2) the depths to chemical and rheological discontinuities and mineral phase boundaries; and (3) depth variations of pressure, temperature, density, and composition. In the absence of seismological data, the most important parameter that permits a rough estimate of how the interior is composed is the average density. Mean density is affected by self-compression, thermal expansion, and pressure-induced mineral phase transitions caused by the weight of overlying layers. In lieu of seismological observations, the determination of a planet's axial moment of inertia, usually by the measurement of the precession rate of the spin axis, provides the principal constraint on the concentration of mass toward the center of the planet. Large-scale gravity and topography data are also important in constraining internal mass distributions since the shapes of the physical surface and the external gravitational field are tied to the radial density distribution and compositionally and/or thermally induced lateral density heterogeneities.

This chapter is arranged as follows: in Section 10.02.2, those observational methods that provide constraints on the interior structure and composition of terrestrial planetary bodies are reviewed. Section 10.02.3 provides the mathematical background for the construction of spherically symmetric density models and discusses thermodynamic equation of state (EOS) parameters relating local density to the prevalent ambient pressure and temperature conditions. Section 10.02.4 describes the interior of the Earth as a type example of a terrestrial planet and is followed by Sections 10.02.5–10.02.8 characterizing in some detail

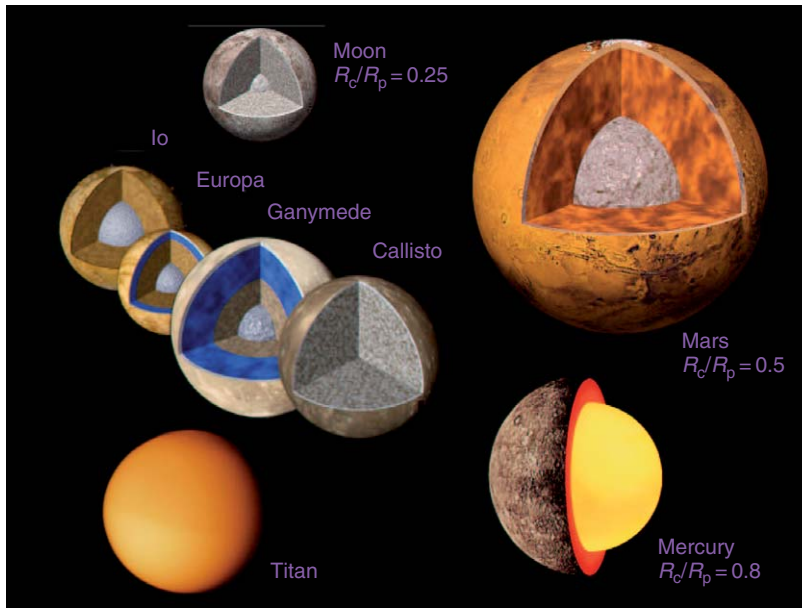


Figure 1 Cut-away views of the interiors of a number of terrestrial-type bodies. R_c/R_p denotes the core radius of a planet or satellite relative to its total radius.

the interiors of the Moon, Mercury, Mars, and Venus. Finally, a summary of this chapter is included in Section 10.02.9.

10.02.2 Observational Methods

Important observational constraints on planetary interiors are provided by astronomical and geodetic methods, rotational and tidal variations, relationships between gravity and topography, magnetic field observations, planetary seismology, interpretations of geologic surface features and compositional variations, and laboratory studies of planetary materials and meteorites.

10.02.2.1 Geodesy

Bulk composition and interior structure of a planet or satellite are mainly constrained by its mean density and mean moment of inertia. The mean density of a planetary body is calculated from its mass and volume. To that end, it is necessary to infer the size and global shape of a planet or satellite from images acquired telescopically using micrometric or photographic techniques or by cameras onboard spacecraft. The global shape or figure of a body depends on its mass, size, rotational and tidal state, and material

strength. Detailed topographic maps of bodies like the Moon, Mars, and Venus have been obtained by using Earth-based radar observations (Muhleman *et al.*, 1995; Margot *et al.*, 1999; Harmon *et al.*, 2001), radio-occultation data, and radar and laser altimetry from orbiting spacecraft (Zuber *et al.*, 1992, 1994; Smith *et al.*, 1999a; Rappaport *et al.*, 1999). Future missions to Mercury also will benefit from laser altimetry (Solomon, 2003). Though the masses of planets and satellites have been known from astronomical observations for a long time, the most current and accurate values are based on measurements of spacecraft that landed, orbited, or flew by.

The gravitational field of a planet or satellite is closely related to the distribution of mass inside the body. Doppler tracking of a spacecraft using its radio communications signal determines its orbit or trajectory from which the gravitational field and the planetocentric constant GM (where G is the universal gravitational constant and M is total mass) can be inferred. The Doppler tracking method is highly accurate in the case of orbiting spacecraft, so that the nominal error of the deduced value of the mean density of the body, for example, $3933.5 \pm 0.4 \text{ kg m}^{-3}$ in the case of Mars, is primarily due to uncertainties in the value of G (Esposito *et al.*, 1992). The mean density is the main indicator of the bulk composition of the terrestrial planets and terrestrial-type bodies.

The density of a material is strongly dependent on porosity and ambient pressure and temperature conditions the latter of which may rise to a few hundreds of GPa and thousands of kelvins deep inside large planets like Venus and Earth. Uncompressed densities vary from about 1000 kg m^{-3} for planetary ices, to 3000 kg m^{-3} for silicate rocks, and up to 8000 kg m^{-3} for metallic iron. The densities of the Moon, the Jovian satellite Io, and the inner terrestrial planets range from about 3300 to 5500 kg m^{-3} , suggesting that the Moon is predominantly composed of rocky material, whereas Mercury mostly consists of metal (**Figure 2**). The Mercury-sized large icy satellites Ganymede, Callisto, and Titan have densities of only about 2000 kg m^{-3} . This implies that ice and rock/metal are present in about equal amounts in their interiors. Enceladus, Triton, Pluto, and Charon are icy bodies with similar ice-rock compositions (**Hussmann et al. 2006**).

The axial moment of inertia of a planet or satellite C can be inferred from the precession of its rotation axis in the presence of external torques exerted on its equatorial bulge. Measurement of the precession rate might require the placement of one or several landers on the surface of the body. For example, the combined analysis of Mars Global Surveyor tracking and Mars Pathfinder and Viking Lander range and Doppler data resulted in an improved value of the moment of inertia (MoI) factor of Mars, that is, the axial moment of inertia

normalized to the planet's mass times its radius squared, $C/MR^2 = 0.3654 \pm 0.0008$ (**Konopliv et al., 2006**). This value is much smaller than the MoI factor of 0.4 of a homogeneous sphere and is consistent with a significant concentration of mass toward the center due to a metallic core with a radius of about half that of the planet (**Schubert and Spohn, 1990; Sohl and Spohn, 1997; Sohl et al., 2005**). The axial moment of inertia of a planetary body can also be deduced from the figure of its gravitational field if the body is in hydrostatic equilibrium. However, this is a demanding requirement that is satisfied by only a few terrestrial-type bodies (see below).

10.02.2.2 Rotation and Tides

The internal mass distribution of a planetary interior can be inferred from its rotational and tidal response to external torques exerted on the planet or satellite (see Chapter 10.04). The torque applied to the body by the gravitational attraction of the Sun or a planet's satellite equals the scalar product of the body's inertia tensor and spin vector. Mercury and Venus have no satellites to affect their rotational states. The combined effect of the torques exerted by the tiny Martian moons, Phobos and Deimos, is much less than the torque exerted on Mars by the Sun (**Van Hoolst et al., 2003**). The torque applied to the Earth by the Moon decelerates the Earth's rotation due to tidal friction in the oceans and, to a minor extent, in the solid Earth (**Platzman, 1984**). In turn, the Moon is accelerated in its orbit and withdraws from Earth at a rate of a few centimeters per year. The rotation axes of Earth and Mars are tilted about axes normal to their orbital planes by 23.45° and 25.2° , respectively, thereby causing their spin axes to precess about the orbit normals under the influence of external gravitational torques.

Astronomical observations have revealed the precession rate of the Earth's spin axis and in turn the Earth's moment of inertia. Radio tracking of the Viking and Mars Pathfinder Landers and Mars Global Surveyor and Mars Odyssey orbiters has yielded similar information for Mars (**Esposito et al., 1992; Folkner et al., 1997; Yoder and Standish, 1997; Yoder et al., 2003; Konopliv et al., 2006**). Laser ranging observations of the Moon, made possible by reflectors placed on the lunar surface during the Apollo program, have determined the Moon's rotational state (**Dickey et al., 1994**). Because of its orbital eccentricity and ellipsoidal shape, the Moon is subject to periodic changes in angular acceleration in response

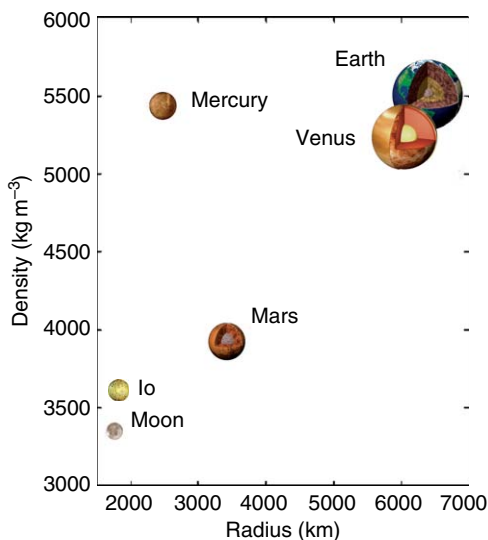


Figure 2 Radius–density relation of the terrestrial planets and the Moon. Note the unusually high mean density of Mercury implying that the planet's interior is predominantly composed of heavy elements such as iron.

to gravitational torques exerted by the Sun and the Earth. The amplitude of the related 27-day forced libration in longitude has been used to infer the moment of inertia of the Moon and the probable molten state of its central region (Yoder, 1981; Williams *et al.*, 2001; Khan *et al.*, 2004). In a similar way, measurements of Mercury's 88-day forced libration amplitude in longitude are expected to provide clues on the planet's internal mass distribution and coupling between core and mantle (Peale, 1976, 1988; Jehn *et al.*, 2004). It is unlikely, however, that the axial moment of inertia of Venus could be derived from observations of its rotational state alone since the planet's retrograde rotation is extremely slow and its rotation axis is more or less perpendicularly aligned to the plane of its nearly circular orbit (Yoder, 1997).

10.02.2.3 Gravity and Topography

Gravimetric and magnetic methods utilize measurements of potential fields in the vicinity of planetary bodies. The long-wavelength part of the external gravitational field provides information on the structure of planetary interiors. Each element of mass in a planet or satellite contributes to the external gravitational field according to Newton's law of gravitation. The gravitational force at a point exterior to the planet can be derived from the gradient or directional derivative of the gravitational potential caused by the total contribution of all mass elements when integrated over the entire volume of the body. In recognition of the first gravity experiments conducted by Galileo Galilei who measured fall times of objects possibly dropped from the Leaning Tower of Pisa, gravitational acceleration is given in units of $1 \text{ mGal} = 10^{-5} \text{ m s}^{-2}$.

The gravitational fields of planetary bodies are measured from orbiting spacecraft. The technique uses the Doppler effect on radio signals transmitted from the Earth to the spacecraft and back. The frequency shift of the radio signals returned by the spacecraft relative to the signal emitted from the ground station is proportional to the velocity component along the direction of vision or line of sight (LOS) and allows the calculation of the LOS acceleration of the spacecraft. These data can be used to calculate the gravitational field at a resolution determined by the altitude and the frequency of signal transmission to the spacecraft. Laser altimetry from orbiting spacecraft has been used to determine the topography of the Moon and Mars with high

accuracy. Radar altimetry data obtained by the Magellan spacecraft have provided topographic maps of Venus. The correlation of topography with the distribution of the Bouguer gravity (gravity corrected for contributions of topographic masses above a well-defined reference level) can be used to infer the degree of isostatic compensation of topography and the depth at which stresses are fully compensated due to rheological and/or compositional changes. Gravity anomalies provide important constraints on elastic lithosphere thickness, crust thickness, crust density, and load density and can be interpreted in terms of chemically or thermally induced lateral and depth variations of density. However, these interpretations suffer from the nonuniqueness inherent in any inversion of the gravity field (*see* Chapter 10.05).

The external gravitational field of a planet or satellite is generally described by a spherical harmonic representation of the gravitational potential as a function of latitude, longitude, and radial distance to the center of mass (CoM). The frequency content of the amplitude spectrum of the gravitational potential gives insight into the rheology and the mechanical and thermal properties of the lithosphere, the outer rigid shell of a planet or satellite. The leading term in the spherical harmonic expansion of the external gravitational potential is the ratio between the planetocentric constant GM and radial distance r representing the gravitational potential of the mass of the body concentrated in a point at its CoM. The next terms of the spherical harmonic representation are inversely proportional to r^3 and involve higher moments of the gravitational field caused by ellipsoidal distortions of the internal mass distribution. The magnitudes of these distortions are related to coefficients $J_2 = -C_{2,0}$ and $C_{2,2}$ for polar oblateness and equatorial ellipticity of the gravitational field, respectively. When the body is in hydrostatic equilibrium, its mean moment of inertia can be deduced from the knowledge of these coefficients with important implications for the internal structure. However, if the lithosphere is thick and strong enough to support stresses associated with surface or subsurface mass anomalies, the planet or satellite may substantially deviate from hydrostatic equilibrium. Furthermore, mantle density anomalies and core-mantle boundary (CMB) undulations may contribute to deviations from hydrostatic equilibrium. Accordingly, the Moon and Mercury are not expected to be fully hydrostatically compensated. The Earth is reasonably close to this state, but Mars is not, due to the uncompensated portion of the

Tharsis uplift. Though the gravitational field of Venus is known quite well, it is not known if the planet is in hydrostatic equilibrium. Therefore, the gravitational field cannot be used to give a reliable value of the planet's moment of inertia. A number of solid bodies in the outer solar system including the large icy satellites of Jupiter and Saturn, Ganymede, Callisto, and Titan, and the strongly tidally heated Jovian satellite Io are likely to be in hydrostatic equilibrium (*see* Chapter 10.15). The quadrupole gravitational fields of these Jovian satellites have been used to infer their moments of inertia (Schubert *et al.*, 2004).

10.02.2.4 Magnetic Fields

Magnetic field observations provide constraints on the interior structure of planets and moons (*see* Chapter 10.07). The existence of an intrinsic planetary magnetic field on a global scale is conclusive evidence that the body has a highly electrically conducting fluid region in its interior within which dynamo action creates the magnetic field. In the case of terrestrial planets the site of magnetic field generation is a metallic core that is at least partially liquid. Earth is the only terrestrial planet with a magnetic field that is unambiguously generated in its core. The nature of Mercury's magnetic field, that is, its mode of origin, is still uncertain though there is no question that Mercury has a large iron core (Schubert *et al.*, 1988). Jupiter's icy satellite Ganymede is the only other terrestrial-like solar system body whose magnetic field is generated by an active liquid metallic core dynamo. The discovery of Ganymede's magnetic field provided crucial evidence that the satellite is differentiated and has a metallic core (Schubert *et al.*, 1996). The absence of a planetary magnetic field, as in the cases of Venus and Mars, only implies the nonexistence of an active dynamo: it does not imply the nonexistence of a metallic core nor does it require a metallic core to be solid.

An external planetary magnetic field can be represented by a spherical harmonic expansion of its magnetic potential in a manner similar to the representation of the gravitational field. It is possible to identify the core dynamo field in the spectrum of the magnetic field spherical harmonic coefficients and thereby determine the radius of the core. This procedure has been used by Voorhies *et al.* (2002) to estimate the radius of Earth's core as 3512 ± 64 km, in good agreement with the seismological radius (*see also* Elphic and Russell, 1978). A similar approach might lead to the determination of the radius of

Mercury's core once future spacecraft have mapped the complete spatial dependence of the planet's magnetic field, assuming that the field originates in a core dynamo.

Though not in possession of global internally generated magnetic fields at present, the Moon (Halekas *et al.*, 2001; Hood *et al.*, 2001; Lin *et al.*, 1998; Russell *et al.*, 1975, 1973) and Mars (Acuña *et al.*, 1999, 1998; Connerney *et al.*, 2004) have localized magnetic fields associated with crustal remanent magnetization. On the assumption that the crustal magnetization was acquired when these bodies had active dynamos in the past, even the crustal magnetization is evidence for the existence of a metallic core in these bodies. This is particularly important for the Moon which has a small metallic core that is difficult to detect by any method. Alternatively, Hood and Huang (1991) have proposed large-scale magnetization in lunar-basin forming impacts caused by plasma-induced antipodal amplification of ambient magnetic fields to explain the correlation of the largest magnetic field strengths with the antipodes of the largest lunar impact basins. The spatial variation of crustal magnetization and its associated magnetic fields also provide information on the internal structure of a body at shallow depth and the internal and surface processes that have affected the crust.

10.02.2.5 Electromagnetics

The phenomenon of electromagnetic induction can be utilized to probe planetary interiors. The method takes advantage of the electrically conducting nature of planetary materials and the time variability of the magnetic fields experienced by planetary bodies. If an electrically conducting object experiences a time-variable magnetic field, electrical currents are induced in the object (Faraday's law of induction). These induced currents in turn generate a magnetic field. If the inducing and induced magnetic fields can be measured, then the electrical conductivity of the object can be inferred. This method has been successfully used to infer the electrical conductivity of the Earth (Banks, 1969; Chapman and Price, 1930; Hobbs, 1987; Lahiri and Price, 1939; Rikitake, 1966; Roberts, 1986; Schuster, 1889; Tarits, 1994) and the Moon (Schubert and Schwartz, 1969; Sonett, 1982; Sonett *et al.*, 1971). It has also been used to find subsurface liquid salt water oceans on the Galilean satellites Europa, Ganymede, and Callisto (Khurana *et al.* 1998; Kivelson *et al.*, 1999, 2000, 2002, 2004; Zimmer *et al.* 2000). In the case of the

Earth, time variations in the external magnetic field are forced by variable ionospheric and magnetospheric current systems. The Moon experiences the variable magnetic field of the solar wind when it is outside the Earth's magnetosphere. The Galilean satellites experience the variability of the rotating, tilted Jovian magnetic field. On Earth, the external forcing magnetic field can be separated from the internal induced magnetic field by a network of surface magnetometers. More recently, satellite data have also been used for this purpose (Olsen 1999; Constable and Constable 2004). For the Moon, magnetometers on the surface and an orbiting spacecraft measured the solar wind forcing field and inductive response during the era of lunar exploration by Apollo spacecraft in the late 1960s and early 1970s. A magnetometer on the Galileo spacecraft measured the induced magnetic fields of Europa, Ganymede, and Callisto. Knowledge of electrical conductivity inside a planetary body indirectly constrains the composition, temperature, and volatile content of the body through the dependence of the conductivity on these properties (Hood, 1986; Hood *et al.*, 1982; Hood and Jones, 1987; Hood and Sonett, 1982; Hood and Zuber, 2000; Sonett *et al.*, 1972). The electromagnetic sounding approach involves two inversion steps, inference of the electrical conductivity from magnetic measurements and inference of composition, temperature, and volatile content from the conductivity.

Magnetic field measurements obtained during the passage of the Moon through the Earth's geomagnetic tail provide a means of detecting the lunar core (Hood *et al.*, 1999). For several days each month the Moon passes through the north and south lobes of the geomagnetic tail and experiences a vacuum-like environment with a near-steady uniform magnetic field. This results in an induced lunar magnetic dipole that acts to exclude the tail lobe field from the Moon's interior. The induced magnetic dipole is produced by electric currents that flow near the surface of the highly electrically conducting metallic core (Hood *et al.*, 1999). The lunar-induced magnetic dipole has been detected by the magnetometer on the Lunar Prospector spacecraft; the measured value of the induced dipole moment implies a core of radius 340 ± 90 km (Hood *et al.*, 1999).

10.02.2.6 Seismology

The propagation of seismic waves following quakes or impacts can be used to infer the structure of planetary interiors. Lognonné (2005) and Lognonné

and Mosser (1993) have provided reviews on planetary seismology (*see* Chapter 10.03). Whereas surface waves are confined to near-surface layers, body waves travel through the interior. The first body waves arriving at a seismic station are longitudinal or P waves that involve material compression and rarefaction. The second are transverse or S waves involving shear motion perpendicular to the direction of propagation. Body waves are subject to reflection, transmission, and conversion from P to S waves and vice versa at internal boundaries at which prominent density and seismic velocity changes occur. A network of at least four seismic stations is required to infer the source location from a comparison of the seismic station records. Free oscillations on a global scale can be excited if the magnitudes of seismic events are sufficiently large. For the Earth, seismology has not only revealed the existence of a metallic core surrounded by a rocky mantle, but it has shown that the core consists of a solid inner core composed of iron and nickel and a liquid outer shell. The analysis of surface waves has provided important clues on the chemical layering of the Earth's crust. Though seismic stations were placed on the Moon's surface during the Apollo exploration era, the collected data are unable to confirm the presence or absence of a small metallic core and do not allow construction of detailed models of the lunar crust and mantle. Seismic instruments placed on the surface of Mars by the Viking mission did not provide data that could be used to determine the planet's internal structure. However, the deployment of seismometers will be central to any future network mission to Mars that attempts to determine the planet's gross interior structure (Lognonné *et al.*, 2000; Dehant *et al.*, 2000). Tidally induced gravity variations raised by Phobos may also permit probing of the deep Martian interior (Van Hoolst *et al.*, 2003).

Promising target bodies for seismic exploration in the outer solar system are the Jovian satellite Europa and the Saturnian satellite Titan due to the likely presence of satellite-wide internal liquid layers beneath the outer ice shells (Grasset *et al.*, 2000; Sohl *et al.*, 2003; Tobie *et al.*, 2005). A passive seismic experiment placed on the surface of Europa would be able to detect seismic activity generated by the formation of cracks, tidally induced quakes, or natural impacts. The thickness of the ice shell could be obtained from low-frequency band observations (0.1–10 Hz) of trapped surface waves (Kovach and Chyba, 2001; Lee *et al.*, 2003).

10.02.2.7 Surface Geology and Composition

The geology and composition of a planet's surface provide important clues into what lies inside the body. These glimpses into the interior, though generally qualitative in nature, are valuable nonetheless and complement more quantitative constraints on internal structure. The basaltic crust of Mercury and the basaltic lowlands of Venus are evidence of the internal differentiation of these bodies. The anorthositic lunar highlands not only attest to the differentiation of the Moon, but they argue for a global-scale magma ocean early in lunar history (Wood *et al.*, 1970; Smith *et al.*, 1970; Warren, 1985). Mercury's high density suggests it is iron rich, yet spectral evidence suggests that its surface is poor in oxidized iron (Vilas, 1985; Blewett *et al.*, 1997), consistent with the segregation of its iron into a central core following differentiation under reducing conditions (Sprague *et al.*, 1994; Schubert *et al.*, 1988).

The crust dichotomy of Mars represents an ancient feature of early Noachian age (>3.5 – 3.7 Gyr ago) that is preserved in the surface geology and tectonics, the cratering record, and the planet's gravity and magnetic field. The heavily cratered southern highlands crust on Mars and the resurfaced northern lowlands of the planet indicate early differentiation and internal dynamical activity (Watters and McGovern, 2005), though removal of the northern crust by one or multiple giant impacts about 4 Gyr ago has also been hypothesized (Wilhelms and Squyres, 1984). However, the detection of quasi-circular depressions in the northern lowlands, interpreted as buried impact craters and basins, suggests a similar age for the lowland and the ancient southern highland crust (Frey *et al.*, 2002). This is in favor of an endogenic origin of the crustal dichotomy involving dynamical processes like degree-1 mantle convection (Schubert and Lingenfelter, 1973; Lingenfelter and Schubert, 1973; Zhong and Zuber, 2001; Roberts and Zhong, 2006), thin-crust formation by early plate tectonics, and the solidification and convective instability of a pristine magma ocean on Mars (Elkins-Tanton *et al.*, 2003b). The ancient dichotomy boundary was modified then by fluvial, aeolian, and glacial processes, as well as by widespread volcanic and sedimentary resurfacing of the northern lowlands (Watters and McGovern, 2005).

Surface geology and signs of endogenic activity are particularly important for inferring the internal structure of outer solar system moons. The heavily

cratered surfaces of Jupiter's icy moon Callisto and Saturn's icy moon Rhea support the inference that Rhea is essentially undifferentiated while Callisto is partially differentiated (ice from rock) (Schubert *et al.*, 2004; Anderson and Schubert, 2007). In contrast, the highly modified surfaces of the Jovian satellites Ganymede and Europa and the Saturnian satellite Enceladus are consistent with the separation of ice and rock in their interiors (Schubert *et al.*, 2004; Porco *et al.*, 2006; Schubert *et al.*, in press). The ubiquitous and ongoing volcanic activity of Jupiter's satellite Io leaves little doubt that the moon has differentiated into an iron-rich core and silicate mantle (Moore *et al.*, 2006). Thermal anomalies detected in Enceladus' south polar region and the active plumes spewing water from beneath the south polar surface of Enceladus (Porco *et al.*, 2006; Spencer *et al.*, 2006) provide additional persuasive evidence for the formation of a rock core and ice mantle inside this body.

While not definitive in themselves, surface geologic and compositional data help to constrain models of planetary and satellite interiors, especially when more quantitative observations are limited.

10.02.2.8 Material Properties

There are only a few kimberlite rock samples brought to the Earth's surface by violent volcanic eruptions that directly probe the deep interior of a terrestrial planet. Diamond deposits occasionally found in kimberlite rocks suggest that confining pressure must have exceeded the pressure at which diamonds are stable. Meteorites originally released from the surfaces of the Moon and Mars during one or several giant impact events represent another important data source on the composition of terrestrial-planet interiors. Much of our knowledge about the interior structure and evolution of the Earth and other terrestrial planets, however, comes from high-pressure mineral physics that includes laboratory experiments and computational studies. Bass (2004) summarizes current and future research activities in this highly interdisciplinary and rapidly evolving field of research (see Volume 2).

Earth and planetary material properties are affected by variable compositions and thermodynamic conditions. The core sulfur content may range from close to eutectic to iron-rich compositions with important implications for the physical state and density stratification of planetary cores (Fei *et al.*, 1995, 1997; Sanloup *et al.*, 2000; Kavner

et al., 2001; Balog *et al.*, 2003) due to the substantial melting point reduction with increasing sulfur concentration (Boehler, 1992, 1996a). Mantle rheology is affected by predominant mineral phase assemblages, water content, and typical mineral grain-size distribution. It is possible that mantle mineralogies of other terrestrial bodies are not dominated by olivine but rather by mixtures of pyroxene minerals. Experimental and theoretical studies of two-phase rheologies (e.g., rock–volatile, rock–melt) are particularly useful for a better understanding of the influence of volatiles like water and carbon and solid gas hydrates on deeply situated geodynamic processes (Sloan, 2003), like the subduction of lithospheric plates on Earth, the rheological behavior of crust and mantle rocks, the kinetics of pressure-induced mineral phase transformations, and the extraction of partial mantle melts (Bass, 2004).

Nowadays, sophisticated tools are available to study the properties of matter under extreme pressure and temperature conditions that prevail in planetary interiors (Liebermann, 2005). From shock and static compression experiments using diamond-anvil facilities, densities, EOS parameters (Hemley and Ashcroft, 1998; Hemley, 2006), and elastic properties of solid mineral phase assemblages (Anderson *et al.*, 1992; Bina and Helffrich, 1992), as well as high-pressure properties of melts (Boehler, 1996b, 1996c) are derived. In these experiments, relatively small samples are subjected to conditions that may prevail deep in the Earth's mantle or even in its metallic core ($P > 135$ GPa, $T > 3000$ K). Future experiments are expected to provide important information on high-pressure transport properties like thermal conductivity and kinematic viscosity, the kinetics of chemical reactions at the CMB, and mineral-phase equilibria up to several tens of GPa. While inelastic X-ray diffraction methods are used to measure sound velocities at very high pressures and temperatures, neutron scattering observations are well-suited to determine the structural properties of silicate melts and aqueous solutions (Bass, 2004). Laboratory experiments need to be augmented by high-performance computations, for example, to simulate diffusion-limited transport processes occurring at atomic scales. These simulations are important to address the influence of oxygen fugacity on mantle rock phase transformation kinetics and the element solubility of light-element admixtures in liquid iron alloys (Badding *et al.*, 1991; Wood, 1993).

10.02.3 Interior Structure and Composition

In the following, we consider two- and three-layer density models before we discuss radially symmetric, depth-dependent models of interior structure.

10.02.3.1 Two- and Three-Layer Structural Models

Models of the internal density distribution of terrestrial planets suffer from an inherent nonuniqueness since there are usually fewer constraints than unknowns. These models are required to satisfy two constraints, the mean density ρ as derived from the total radius R and mass M_p and the mean moment of inertia I that can be determined from the quadrupole moments of the gravitational field and the frequency of precession of the rotation axis.

Given the paucity of information available, three-layer models representing the core, the mantle, and the crust can be considered as useful approximation to the structure of terrestrial-planet interiors. The corresponding structural equations are given by

$$\rho = \rho_s + (\rho_c - \rho_m) \left(\frac{R_c}{R} \right)^3 + (\rho_m - \rho_s) \left(\frac{R_m}{R} \right)^3 \quad [1]$$

$$\frac{I}{MR^2} = \frac{2}{5} \left(\frac{\rho_s}{\rho} + \frac{\rho_c - \rho_m}{\rho} \left(\frac{R_c}{R} \right)^5 + \frac{\rho_m - \rho_s}{\rho} \left(\frac{R_m}{R} \right)^5 \right) \quad [2]$$

where the core radius R_c , the crust–mantle radius R_m , the crust density ρ_s , the mantle density ρ_m , and the core density ρ_c are unknown. Even two-layer interior structure models lacking a crust layer ($\rho_s = 0$, $R_m = R$) would have fewer constraints than unknowns, that is, ρ_c , R_c , and ρ_m .

The mean density of a two-layer spherical body is given by

$$\rho R^3 = (\rho_c - \rho_m) R_c^3 + \rho_m R^3 \quad [3]$$

from which the relative core radius R_c/R , core mass fraction M_c/M_p , and dimensionless mean MoI factor are obtained according to

$$\frac{R_c}{R} = \left(\frac{\rho - \rho_m}{\rho_c - \rho_m} \right)^{1/3} \quad [4]$$

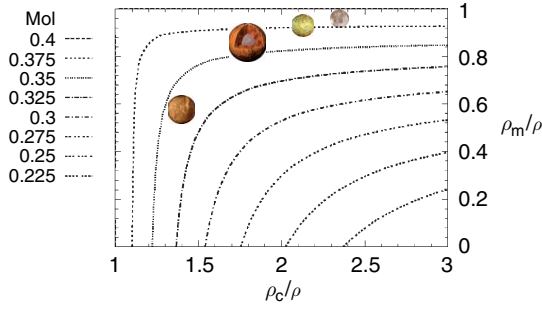


Figure 3 Contours of the mean moment-of-inertia factor MoI for two-layer structural models of planetary interiors as a function of core and mantle density ρ_c and ρ_m , respectively, relative to mean density ρ . The symbols shown in the diagram represent putative locations of the Moon, Io, Mars, and Mercury.

$$\frac{M_c}{M_p} = \frac{\rho_c}{\rho} \left(\frac{R_c}{R_p} \right)^3 = \frac{\rho_c (\rho - \rho_m)}{\rho (\rho_c - \rho_m)} \quad [5]$$

and

$$\text{MoI} = \frac{I}{M_p R^2} = \frac{2}{5} \left(\frac{(\rho - \rho_m)^{5/3}}{\rho (\rho_c - \rho_m)^{2/3}} + \frac{\rho_m}{\rho} \right) \quad [6]$$

respectively. If hydrostatic equilibrium is assumed, the corresponding increase of density with depth is equivalent to the requirement $\rho_c \geq \rho$ and $0 \leq \rho_m \leq \rho$. In **Figure 3**, contours of MoI are shown for plausible ranges of core and mantle densities normalized to the mean density, ρ_c/ρ and ρ_m/ρ , respectively.

10.02.3.2 Multilayer Structural Models

A commonly used approach to modeling the interior structure of a terrestrial planet given its mass, radius, and moment of inertia (see [Wood et al. \(1981\)](#) for a review) converts the estimated bulk composition into a mineralogical model and adopts potential temperatures for the mantle layers and the core from thermal history calculations. The potential temperature is the temperature extrapolated adiabatically to the surface pressure. The radial density distribution is then calculated under the assumption of hydrostatic and thermal equilibrium using an EOS to correct for compression and thermal expansion. The total mass and the MoI are calculated from the model and compared with the data. This approach can be modified by simultaneously calculating the thermal and mechanical structure of a terrestrial body ([Sohl and Spohn, 1997](#)). In order to derive a self-consistent structural model, STP values of the density, the

bulk modulus, and the thermal expansivity are calculated from laboratory data for the individual layers of the model.

10.02.3.2.1 Governing equations

If a spherically symmetric planet in perfect mechanical and thermal equilibrium is assumed, the following set of differential equations for mass m , iron mass m_{Fe} , mean moment of inertia θ , acceleration of gravity g , pressure p , and heat flux q can be derived from fundamental principles:

$$\frac{dm}{dr} = 4\pi r^2 \rho_r \quad [7]$$

$$\frac{dm_{\text{Fe}}}{dr} = x_{\text{Fe}} \frac{dm}{dr} \quad [8]$$

$$\frac{d\theta}{dr} = \frac{8}{3} \pi r^4 \rho_r \quad [9]$$

$$\frac{dg}{dr} = 4\pi G \rho_r - 2 \frac{g}{r} \quad [10]$$

$$\frac{dp}{dr} = -\rho_r g \quad [11]$$

$$\frac{dq}{dr} = \rho_r \varepsilon_r - 2 \frac{q}{r} \quad [12]$$

where r is the radial distance from the center of the planet, G is the gravitational constant, ρ is the density, x_{Fe} is the concentration of iron per unit mass, and ε is the specific heat production rate. The subscript r indicates quantities that are local functions of p , T , and composition.

The mean MoI factor $I/M_p r_p^2$ should be used for the construction of spherically symmetric models and can be derived from the planet's observed polar MoI factor $C/M_p r_p^2$ and the second-degree coefficients of the spherical harmonic representation of its gravitational field, \mathcal{F}_2 and $\mathcal{F}_{2,2}$. The mean and polar MoI factors are related to each other by

$$\frac{I}{M_p r_p^2} = \frac{C}{M_p r_p^2} - \frac{2}{3} \mathcal{F}_2 = \frac{C}{M_p r_p^2} + \frac{2}{3} C_{2,0} \quad [13]$$

where

$$\mathcal{F}_2 = \frac{1}{M_p r_p^2} \left[C - \frac{A+B}{2} \right] = -C_{2,0} \quad [14]$$

is the planet's gravitational oblateness and $A < B < C$ are the planet's principal equatorial and polar moments of inertia, respectively. A more comprehensive account including minor nonhydrostatic corrections to the mean MoI factor due to symmetric distributions of topographical masses like, for

example, the Tharsis rise on Mars is provided by [Sohl *et al.* \(2005\)](#).

The base of the rheological lithosphere is defined with the help of the temperature T_{rheo} at which subsolidus creep becomes effective over geologic timescales and which is taken as 0.6 times the solidus temperature T_m ([Meissner and Vetter 1979](#)) or about 800°C. The rheological lithosphere is the upper part of the thicker thermal lithosphere which additionally comprises the upper cold thermal boundary layer of the convecting mantle and thus represents the thermally conductive outermost layer of the planet ([Spohn, 1991](#)). The boundary temperature at the base of the thermal lithosphere T_{lith} is taken to be $0.85 T_m$ ([Ranalli 1987](#)) or about 1400°C. There is an additional core–mantle thermal boundary layer at the bottom of the mantle. The thickness δ of the CMB layer is calculated from the local critical Rayleigh number for marginal stability of the layer. The local critical Rayleigh number is ([Jarvis and Peltier, 1989](#))

$$Ra_c = \frac{g\alpha}{\kappa\nu k} q_b \delta^4$$

where κ is the thermal diffusivity, α is the thermal expansivity, and the kinematic viscosity ν is evaluated at the geometrically averaged temperature of the boundary layer; q_b is the sum of the basal heat flux and the heat production rate per unit area $\rho\epsilon\delta$ and k is the thermal conductivity. Within the boundary layers, heat is transported radially by conduction and the temperature T satisfies

$$\frac{dT}{dr} = -\frac{q}{k_r} \quad [15]$$

Between the boundary layers energy is primarily carried by convection and the temperature gradient is assumed to be approximately equal to the adiabatic temperature gradient ([Stacey, 1977](#))

$$\frac{dT}{dr} = T \frac{\gamma_r}{K_{S,r}} \frac{dp}{dr} \quad [16]$$

where $\gamma = \alpha K_S / \rho c_p$ is the thermodynamic Grüneisen parameter, and K_S is the adiabatic bulk modulus.

The radial positions of pressure-induced mantle phase boundaries like the exothermic olivine– β -spinel and β -spinel– γ -spinel transitions and the endothermic γ -spinel–perovskite transition, can be obtained from the intersections of the temperature profile calculated from eqns. [12] through [16] and the specific Clausius–Clapeyron curves.

The set of basic differential equations [7]–[16] can be separated into two subsets that are coupled through the density ρ . The mechanical properties of the interior are calculated from eqns [7]–[11], while eqns. [12]–[16] give the thermal structure of the model. Because ρ depends more strongly on pressure than on temperature, a feature common to most planetary bodies, except the strongly tidally heated Jovian satellite Io and perhaps the Earth’s Moon, it is possible to calculate the density distribution by using an isothermal fourth-order Eulerian finite strain–Murnaghan–Birch EOS and by applying temperature corrections through a calculation of the thermal pressure as described further below ([Stacey *et al.*, 1981](#)) and illustrated in [Figure 4](#).

10.02.3.2.2 Equation of state

STP parameter values of density ρ_{ref} , mean atomic mass $\bar{\mu}$, thermal expansivity α_{ref} , isothermal bulk modulus $K_{T,\text{ref}}$, and rigidity G_{ref} of an assemblage of n components can be calculated from

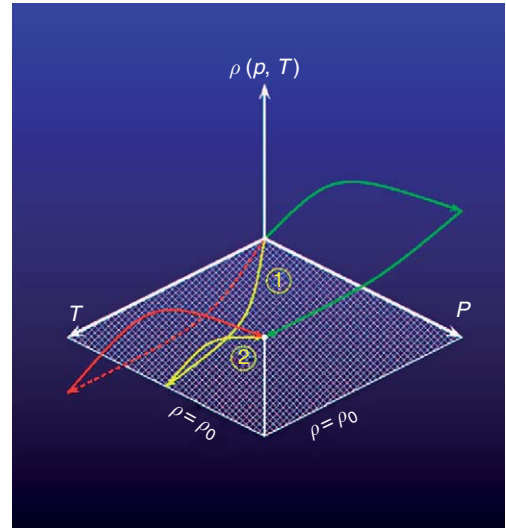


Figure 4 Schematic view of the extrapolation of density $\rho(p, T)$ to elevated pressures p and temperatures T . The origin of the coordinate system refers to an arbitrarily chosen reference density $\rho_0(p_0, T_0)$ at fixed (standard) pressure and temperature conditions p_0 and T_0 , respectively. First the increase of thermal pressure caused by thermal expansion is calculated (path 1), then the isothermal Birch–Murnaghan equation (path 2) is applied to account for pressure-induced compression. Also shown are alternate thermodynamic paths. Adapted from Wood JA, Anderson DL, Buck WR *et al.* (1981) Geophysical and cosmochemical constraints on properties of mantles of the terrestrial planets. In: Kaula WM (ed.) *Basaltic Volcanism on the Terrestrial Planets*, pp. 633–699. New York: Pergamon.

volume-weighted averages applying the widely used Voigt–Reuss–Hill method (Watt *et al.*, 1976):

$$\rho_{\text{ref}} = \left(\sum_{i=1}^n \frac{x_i}{\rho_i} \right)^{-1} \quad [17]$$

$$\bar{\mu} = \left(\sum_{i=1}^n \frac{x_i}{\mu_i} \right)^{-1} \quad [18]$$

$$\alpha_{\text{ref}} = \rho_{\text{ref}} \sum_{i=1}^n \frac{x_i \alpha_i}{\rho_i} \quad [19]$$

$$K_{T,\text{ref}} = \left(\rho_{\text{ref}} \sum_{i=1}^n \frac{x_i}{\rho_i K_{T,i}} \right)^{-1} \quad [20]$$

$$G_{\text{ref}} = \left(\rho_{\text{ref}} \sum_{i=1}^n \frac{x_i}{\rho_i G_i} \right)^{-1} \quad [21]$$

where x_i is the mass fraction of an individual crust, mantle, or core component with STP density ρ_i , mean atomic mass $\bar{\mu}_i$, thermal expansivity α_i , isothermal bulk modulus $K_{T,i}$, and rigidity G_i . This is the simplest bounding method that is preferentially applied to isotropic composites by calculating arithmetic means of bounds in which stresses (Reuss bound) and strains (Voigt bound) are assumed to be uniform. For two-phase composites and polycrystals, however, Hashin–Shtrikman bounds are preferred over the Voigt–Reuss–Hill average (Watt *et al.*, 1976).

Since internal temperatures of the terrestrial-type bodies exceed the Debye temperature, the quasi-harmonic approximation is valid and the product of thermal expansivity α and isothermal incompressibility K_T

$$\alpha K_T = - \left(\frac{1}{\rho} \frac{\partial \rho}{\partial T} \right)_p \times \left(\rho \frac{\partial p}{\partial \rho} \right)_T = \left(\frac{\partial p}{\partial T} \right)_V \quad [22]$$

can be considered to be constant throughout chemically homogeneous layers (Anderson *et al.*, 1992). Under these circumstances, the thermal pressure (cf. Figure 4, path 1)) is given by

$$p_{\text{th}} = \int_{T_{\text{ref}}}^T \left(\frac{\partial p}{\partial T} \right)_V dT = \int_{T_{\text{ref}}}^T \alpha K_T dT \approx \alpha_{\text{ref}} K_{T,\text{ref}} (T - T_{\text{ref}}) \quad [23]$$

and can be used to include the temperature effect in the EOS parameters (Anderson, 1984).

From the thermodynamic identity (Anderson, 1989)

$$\left(\frac{dM}{dT} \right)_V = \left(\frac{dM}{dT} \right)_p + \alpha K_T \left(\frac{dM}{dp} \right)_T \quad [24]$$

for any thermodynamic function M and Swenson's law (Anderson *et al.*, 1992)

$$\left(\frac{dK_T}{dT} \right)_V = 0 \quad [25]$$

the first temperature derivatives $(dK_T/dT)_p$, $(d\alpha/dT)_p$, and $(dG/dT)_p$ used at constant pressure in the high-temperature limit for making linear temperature corrections to the EOS parameters can be attributed to well-known physical properties under STP conditions according to

$$\left(\frac{dK_T}{dT} \right)_p = -\alpha_{\text{ref}} K_{T,\text{ref}} \left(\frac{dK_T}{dp} \right)_{\text{ref}} \quad [26]$$

$$\left(\frac{d\alpha}{dT} \right)_p = \alpha_{\text{ref}}^2 \left(\frac{dK_T}{dp} \right)_{\text{ref}} \quad [27]$$

$$\left(\frac{dG}{dT} \right)_p = -\alpha_{\text{ref}} G_{\text{ref}} \left(\frac{dK_T}{dp} \right)_{\text{ref}} \quad [28]$$

where $(dK_T/dp)_{\text{ref}}$ is the first pressure derivative of the isothermal bulk modulus as obtained from Voigt–Reuss–Hill averaging over individual components in the reference state. Furthermore, the first pressure derivative of rigidity is simply taken as (Poirier and Liebermann 1984)

$$\left(\frac{dG}{dp} \right)_{\text{ref}} = \frac{G_{\text{ref}}}{K_{T,\text{ref}}} \left(\frac{dK_T}{dp} \right)_{\text{ref}} \quad [29]$$

Using the truncation in Eulerian strain at fourth order, we subsequently infer the pressure dependence of the elastic moduli G and K_T and its local pressure derivative dK_T/dp (Stacey *et al.*, 1981; Bina and Helffrich, 1992):

$$K_T = K_{T,0} (1 - 2f)^{5/2} \left\{ 1 - f \left(5 - 3 \left(\frac{dK_T}{dp} \right)_{\text{ref}} \right) + \frac{f^2}{2} \left[9K_{T,0} K_{T,0}'' + \left(3 \left(\frac{dK_T}{dp} \right)_{\text{ref}} - 7 \right) \times \left(3 \left(\frac{dK_T}{dp} \right)_{\text{ref}} - 5 \right) \right] \right\} \quad [30]$$

$$G = G_0 (1 - 2f)^{5/2} \left\{ 1 - f \left(5 - 3 \left(\frac{dG}{dp} \right)_{\text{ref}} \frac{K_{T,0}}{G_0} \right) + \frac{f^2}{2} \left[9G_0^2 \frac{K_{T,0}^2}{G_0} + 9 \left(\frac{dG}{dp} \right)_{\text{ref}} \frac{K_{T,0}}{G_0} \times \left(\left(\frac{dK_T}{dp} \right)_{\text{ref}} - 4 \right) + 35 \right] \right\} \quad [31]$$

$$\frac{dK_T}{dp} = \left(\frac{dK_T}{dp} \right)_{\text{ref}} + 3K_{T,0}K''_{T,0}f \quad [32]$$

with

$$f = \frac{1}{2} \left[\left(\frac{\rho}{\rho_0} \right)^{2/3} - 1 \right] \quad [33]$$

where the double prime indicates the second derivative with respect to pressure. Since reliable measurements of $K''_{T,0}$ and G''_0 are not readily available for terrestrial mantle rocks, one may assume

$$G''_0 \frac{K_{T,0}^2}{G_0} \approx -\frac{35}{9} \quad [34]$$

and (Hofmeister, 1991)

$$K_{T,0}K''_{T,0} \approx -\left(\frac{dK_T}{dp} \right)_{\text{ref}}^2 + 7\left(\frac{dK_T}{dp} \right)_{\text{ref}} - \frac{143}{9} \quad [35]$$

Consequently, the pressure effect on density is attributed to isothermal compression (cf. Figure 4, path 2) and, finally, eqns [30] and [33] are iteratively solved for local density ρ .

To calculate the seismic structure of the interior in terms of the P- and S-wave velocities

$$v_p = \sqrt{\frac{K_S + (4/3)}{\rho}} \quad [36]$$

and

$$v_s = \sqrt{\frac{G}{\rho}} \quad [37]$$

the isothermal–adiabatic transformation

$$\frac{K_S}{K_T} = 1 + \gamma\alpha T \quad [38]$$

between adiabatic bulk modulus K_S and its isothermal counterpart K_T is employed by using Slater's formulation

$$\gamma \approx \frac{1}{2} \frac{dK_T}{dp} - \frac{1}{6} \quad [39]$$

as an approximation of the thermal Grüneisen parameter γ (Stacey, 1977).

10.02.3.2.3 Boundary conditions

The set of basic differential equations [7]–[16] can be solved by numerical integration with respect to the following boundary conditions. The central boundary conditions at $r=0$ are

$$\begin{aligned} m &= 0 \\ m_{\text{Fe}} &= 0 \\ \theta &= 0 \\ g &= 0 \\ p &= p_c \\ q &= 0 \\ T &= T_c \end{aligned} \quad [40]$$

Since there are three observational constraints on the model, the mass, the radius, and the polar moment of inertia or the global Fe/Si ratio, respectively, we can choose three parameters as adjustable, the values of which are iteratively adjusted such that the observational constraints can be satisfied. These parameters are the central pressure p_c , the central temperature T_c , and the pressure at the core–mantle boundary p_{cmb} .

The surface boundary conditions at $r=r_p$ are

$$\begin{aligned} m &= M_p \\ m_{\text{Fe}} &= M_{\text{Fe}} \\ \theta &= I \\ g &= g_p \\ p &= p_p \\ q &= q_p \\ T &= T_p \end{aligned} \quad [41]$$

where the mean moment of inertia I can be approximately given by the polar moment C . While the mass M_p and the mean surface values of gravity g_p , pressure p_p and temperature T_p have been derived from spacecraft and Earth-based observations, the surface heat flux q_p values of almost all terrestrial bodies are unknown at present. Therefore, the boundary condition for the heat flux density is taken at the core–mantle boundary rather than at the surface. This is convenient because the heat flux in the mantle and in the crust depends on the bulk chemistry. The heat flow from the core into the base of the mantle q_{cmb} strongly depends on the thermal history of the core and can be assessed from thermal history calculations (see Chapter 10.09).

10.02.3.2.4 Numerical solution

A modified predictor–corrector integration scheme using the Adams–PECE method (Shampine and Gordon, 1975) is suitable to numerically solve eqns [7]–[16]. Furthermore, a shooting method using multidimensional globally convergent Newton–Raphson

iteration (Press *et al.*, 1992) can be employed in order to simultaneously adjust the free parameters of the system, for example, ρ_c , T_c , ρ_{cmb} , ρ_{cr} , q_p , and the global ratio Fe/Si or the MoI factor $C/M_p r_p^2$. Integration proceeds from the center outwards and, at the same time, from the surface inwards. The solutions are required to match at an arbitrarily chosen matching point within a prescribed numerical accuracy limit. If present, the olivine–spinel transition may serve as matching point with continuous iteration until the successful solution requiring continuity of all components is met at the internal fitting point within the numerical accuracy limit. For the sake of rapid convergence to the successful solution, the initial set of starting parameters is constrained to lie sufficiently close to the final set of parameters. An educated guess of the initial set can be obtained by using the above analytical solutions for a three-layer structural model having the planet's mass, iron mass fraction, basaltic crust density, and homogeneously distributed crust/mantle heat sources.

10.02.4 Earth as a Type Example of a Terrestrial Planet

Inferences about the structure, composition, and mineralogy of the planets are guided by our knowledge of the Earth. In some cases, Venus for example, observational constraints on the interior are so minimal that the best we can do is to argue by analogy with Earth. Our knowledge of Earth's interior, though partially based on the same types of observations available for the planets, rests largely on seismological data. The Moon is the only planetary body other than Earth for which we have seismological data and those data are limited in both quality and quantity. The structure, composition, and mineralogy of the Earth are discussed at length in other volumes of this treatise (see Volumes 1 and 2) and in the *Treatise of Geochemistry* (see Volumes 1–3.) The brief summary we present here is intended only to place the blurry pictures of planetary interiors in the context of the sharper picture of Earth's interior.

10.02.4.1 General

The basic structure of the Earth is that of a three-layer sphere. The innermost layer is a metallic core of radius 3486 km. Surrounding the core is a rocky spherical shell or mantle of thickness 2885 km and encircling the mantle is a thin rocky crust distinct in

composition from the underlying mantle. The core is itself divided into two parts, an inner solid core of radius 1217 km surrounded by an outer liquid shell about 2269 km thick. It is believed that the inner core has formed as a consequence of the cooling of the Earth over geologic time, a process that has resulted in the partial solidification of the core from the inside out. The mantle is itself divided into two parts, the upper mantle about 660 km thick and the lower mantle about 2225 km thick. The mantle subdivisions are based on the occurrence of solid–solid phase transitions in the mantle rock, about which more is discussed below. The crust is neither uniform in composition or thickness. An approximately 6-km-thick crustal layer covers the floors of the oceans while a compositionally distinct crust of about 30 km thickness comprises the continents. The basic structure of the Earth is shown in Figure 5.

10.02.4.2 Interior Structure

The overall structure of the Earth is generally believed to have been set early in Earth's evolution, within tens to about 100 Myr after accretion was complete (see Volume 9). The gravitational potential energy released upon accretion was large enough to melt the Earth's interior yielding liquid metal, mostly iron, that sank toward the center and accumulated to form the metallic core. The process of core formation could have begun before accretion was complete. Core formation itself releases additional energy that

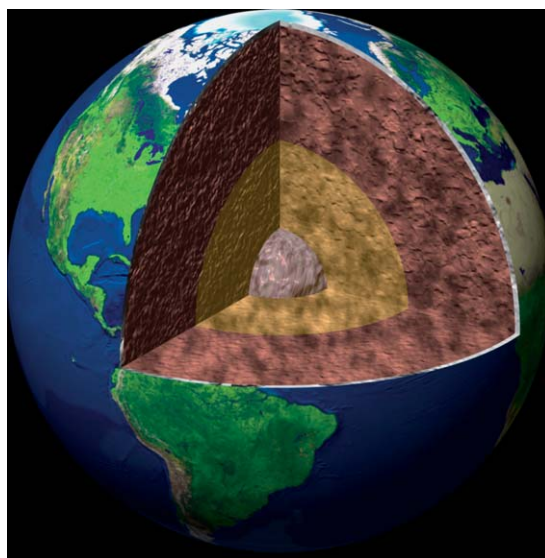


Figure 5 Cut-away view of the Earth's interior. © Calvin J. Hamilton.

could have contributed to melting the mantle. Formation of the core could have been a runaway process. The timing of crustal formation is more uncertain. Certainly, oceanic crust (basalt) is being produced today by melting of mantle rocks at mid-ocean ridges. This process has occurred throughout Earth's history, as long as plate tectonics has been active. Basaltic volcanism does not require plate tectonics, as is evident from the surfaces of other planets, so basaltic crust was likely produced on Earth early in its evolution by plate tectonics or other processes. Oceanic crust is recycled back into the mantle by plate tectonics. The oldest oceanic crust on Earth is only about 200 Myr. The more difficult problem in crustal evolution is the history of the continental crust. The more siliceous continental crust is believed to have been produced by multiple stages of melting in the presence of water. The process is occurring in the andesitic volcanoes at convergent plate margins. The main question is how much continental crust existed on Earth as a function of time throughout Earth's history (*see* Chapter 9.07).

10.02.4.3 Composition

The bulk composition of the Earth, aside from its volatiles, is believed to be that of the meteorites classified as CI chondrites, the assumed primordial building blocks of the Earth. Accordingly, the Earth is 32.7 wt.% Fe, 15.4 wt.% Mg, 14.2 wt.% Si, 1.89 wt.% Ni, 1.71 wt.% Ca, and 1.59 wt.% Al (McDonough and Sun, 1995). Other elements are of course present in relatively smaller amounts. Much of the Earth's Fe and Ni has segregated into the core which contains about 87.5 wt.% Fe, 5.4 wt.% Ni, 0.95 wt.% Cr, 0.5 wt.% Mn, and unknown amounts of light elements such as O and S (McDonough and Sun, 1995). The light elements of the core are preferentially excluded from the inner core upon its solidification and concentrated in the liquid outer core. The major elements of the mantle rocks, aside from volatiles, are Mg (22.8 wt.%), Si (21.0 wt.%), Fe (6.26 wt.%), Ca (2.53 wt.%), and Al (2.35 wt.%) (McDonough and Sun, 1995). The composition of the mantle is also constrained by its density, seismic velocities, seismic anisotropy, and the compositions of ophiolite complexes and mantle xenoliths brought to the surface by kimberlitic and alkali basaltic eruptions. The elements of the mantle are contained in the minerals olivine ((Mg, Fe)₂SiO₄), orthopyroxene ((Mg, Fe)SiO₃), clinopyroxene (([Ca, Mg]₂, NaAl)Si₂O₆), and garnet

((Mg, Fe, Ca)₃Al₂Si₃O₁₂). Olivine is a complete solid solution of Mg and Fe silicates with end members fayalite (Fe₂SiO₄) and forsterite (Mg₂SiO₄). Orthopyroxene is a limited solid solution with magnesium end member enstatite (the Fe end member is unstable). Clinopyroxene is a pyroxene solid solution with Ca and Al. Among all possible rock assemblages of these minerals only peridotites (olivine + pyroxene) and eclogites (pyroxene + garnet) are commonly found in mantle-derived samples. Eclogite is isochemical with basalt and transforms to basalt at depths of less than about 80 km in the Earth. The mineralogy and composition of the Earth's mantle might be that of pyrolite, a peridotite model introduced by Ringwood (1975) to explain the seismic, petrologic, and mineralogic properties of the upper mantle.

10.02.4.4 Mineralogy

Olivine and pyroxene transform to higher-density polymorphs under the high temperatures and pressures encountered at depth in the Earth's mantle. At a depth of about 410 km olivine transforms to spinel (the transformation occurs in two steps involving wadsleyite, or β -spinel, and at higher pressure ringwoodite, or γ -spinel). A prominent seismic discontinuity at the depth of about 410 km is believed associated with the olivine–spinel phase change. This subsolidus phase change is exothermic and involves jumps in seismic velocities and density. Another major seismic discontinuity occurs at the depth of about 660 km and this is believed to coincide with the transformation of ringwoodite to magnesium perovskite and magnesiowüstite. This solid–solid phase transformation is endothermic. The region between 410 km depth and 660 km depth is known as the transition zone. The depth of 660 km marks the boundary between the upper mantle and the lower mantle. Perovskite-forming reactions also occur in the pyroxene system but over a wider pressure interval than in the olivine system. Garnet, for example, dissociates to form MgSiO₃ and CaMgSiO₃ perovskites plus Al₂O₃. The lower mantle is thus dominated by silicate perovskites.

Recent laboratory and theoretical results have demonstrated that perovskite transforms to still another structure, post-perovskite, at pressures and temperatures found just above the core–mantle boundary in the Earth (Murakami *et al.*, 2004; Oganov and Ono, 2004; Tsuchiya *et al.*, 2004). The perovskite–post-perovskite transformation, like the

olivine–spinel phase change, is an exothermic reaction. The location of this phase transition is coincident with the several hundred kilometer thick layer at the bottom of the mantle known as the D''-layer wherein seismic velocities undergo large variations (Lay *et al.*, 2005).

The subsolidus phase changes in the Earth's mantle have important effects on the dynamics of the mantle (Schubert *et al.*, 2001). The exothermic reactions generally promote convection while the endothermic phase change retards it. Do similar phase changes occur in other terrestrial planets? Venus is large enough that the olivine–spinel and spinel–perovskite phase changes should be present in its mantle. However, the pressure at the base of Venus's mantle may not be sufficiently high for the occurrence of the perovskite–post-perovskite phase change. Mars is so small that only the olivine–spinel phase change might occur near the base of its mantle. Possible phase changes in the mantles of the other planets will be discussed in more detail below.

10.02.5 The Moon

The Moon is one of the best-understood bodies in the solar system. The first billion years of the impact history of the Earth–Moon system are retained in the lunar crater record. The chronology of major impact events has been derived from rock and soil samples collected during the Apollo and Luna missions and represents the current-best database for dating other planetary surfaces in the solar system (Kaula *et al.*, 1986). A number of lunar meteorites provide additional constraints on the early evolution and bulk composition of the lunar crust (Korotev, 2005).

10.02.5.1 General

The Clementine and Lunar Prospector missions have returned global data sets of lunar gravity, topography, remanent magnetism, mineralogy, and chemical composition of the surface (Nozette *et al.*, 1994; Binder, 1998). The low mean lunar density implies that the Moon is depleted in iron relative to the other terrestrial planets. Dynamical modeling and isotopic data suggest that accretion and differentiation occurred soon after the formation of a vapor and debris cloud caused by the giant impact of a Mars-sized planetesimal into the early Earth. The internal differentiation of the Moon was accompanied by the formation of a magma ocean subsequent to hot

accretion and extraction of a highly aluminous flotation crust enriched in plagioclase feldspar (Wood *et al.*, 1970; Smith *et al.*, 1970; Warren, 1985). The duration and depth of differentiation during the magma-ocean phase, the possible existence of an undifferentiated lower mantle, and the mechanism of core formation are among the key questions of lunar science (Jolliff *et al.*, 2000b). For review articles on the internal constitution and thermal–magmatic evolution of the Moon, we refer the reader to Wieczorek *et al.* (2006) and Shearer *et al.* (2006), respectively.

10.02.5.2 Interior Structure

Models of the layering and composition of the lunar interior are widely based on the Apollo lunar seismic data combined with measurements of the mean density and the MoI factor. Seismic measurements at the Apollo 12, 14, 15, and 16 landing sites indicate that the lunar interior consists of a crust and a mantle. The chemical composition of the silicate mantle is consistent with that of an olivine–pyroxene mixture (Toksöz *et al.*, 1974; Hood and Jones, 1987). From Doppler tracking of the Lunar Prospector spacecraft and lunar laser ranging data on lunar libration, Konopliv *et al.* (1998) have inferred an improved average MoI factor of $I_p/M_p r_p^2 = 0.3931 \pm 0.0002$ and Konopliv *et al.* (2001) have derived a lunar tidal potential Love number of $k_2 = 0.026 \pm 0.003$. Despite the improved values of the moment of inertia and tidal potential Love number, models of the lunar interior are nonunique. Considerable uncertainty is connected with the radius and physical state of a possible metallic core, more gradual or discontinuous seismic velocity variations within the lunar mantle, and lateral and vertical heterogeneities of the lunar crust, the mean thickness of which is estimated at 49 ± 15 km if an Airy-type compensation mechanism applies (Wieczorek *et al.*, 2006).

Lunar laser ranging data show that the true spin axis of the Moon is displaced from the Cassini alignment (mean direction of the spin axis) by 0.26 arcsec. This can be explained by internal dissipation in the presence of a fluid core (Yoder, 1981; Dickey *et al.*, 1994; Williams *et al.* 2001). Furthermore, the paleomagnetic record of some lunar samples suggests the former existence of a significant magnetic field produced by dynamo action in a liquid metallic core (Hood and Jones, 1987). However, the size of a possible lunar core is less well determined. The seismic data allow the existence of a lunar core with

a radius of 170–360 km (Nakamura *et al.*, 1974). The MoI factor determined by Konopliv *et al.* (1998) is consistent with a core radius between 220 and 450 km. Furthermore, independent observations of the lunar magnetic moment induced in the geomagnetic tail of the Earth suggest that the lunar core radius is 340 ± 90 km (Hood *et al.*, 1999). A combined analysis of mean density, MoI factor, tidal potential Love number k_2 , and quality factor Q and the inversion of the entire set of lunar laser ranging and seismic data implies a molten or partially molten iron core with radius and density of about 350 km and 7200 kg m^{-3} , respectively (Khan *et al.*, 2004). The possible range of density models that simultaneously satisfy the mean density and moment of inertia of the Moon are shown in Figure 6.

10.02.5.3 Composition

The lunar surface is divided into light-colored heavily cratered highlands and smooth dark lowland maria which are most prominent on the near side. The highlands are saturated with large craters owing to their greater age in comparison to the maria and dominate the lunar far side and most of the near side. Highly anorthositic rocks are exposed in the lunar highlands, whereas the maria represent floods of basaltic lava that were erupted about 0.5 Gyr after major impact events. Little mare volcanism is associated with the South Pole Aitken basin, and Oceanus Procellarum, the largest expanse of mare volcanism,

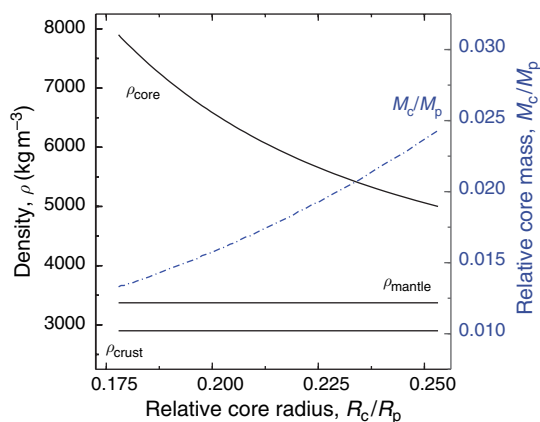


Figure 6 Three-layer model determinations of lunar mantle and core density and core mass fraction M_c/M_p vs relative core radius R_c/R_p consistent with the mean density and MoI factor of the Moon. The thickness and density of the anorthositic lunar crust is fixed at 60 km and 2900 kg m^{-3} , respectively.

is not necessarily associated with an impact event (Neumann *et al.*, 1996).

It appears that the majority of the lunar basalts erupted within the Procellarum-KREEP-Terrane (Jolliff *et al.*, 2000a), a unique geologic province that contains elevated abundances of heat-producing elements. Wiczorek and Phillips (2000) have shown that the enhanced heat production of this province could have melted the underlying mantle. Wiczorek *et al.* (2001) have suggested that mare basalts might preferentially erupt within the impact basins since mare basalts are more dense than the upper anorthositic crust, but less dense than the deep, more mafic, lower crust. If an impact event stripped away the upper crust, mare basalts could easily rise through the crust and erupt based solely on buoyancy considerations. The compositions of the mare basalts are consistent with volcanic source regions of several hundred kilometers depth (Heiken *et al.*, 1991). Mare basalt samples provide an assessment of the Mg number $\text{MgO}/(\text{MgO} + \text{FeO})$ of 0.75–0.8 and a bulk Al_2O_3 content of 1 wt.% for the upper mantle (Hood and Zuber, 2000). The ages of the basaltic maria, as determined from returned samples and careful crater chronologic studies, range between about 4 and ≈ 1.2 Gyr (Hiesinger *et al.*, 2003) and suggest that U-, Th-, and K-rich residua of the crystallized magma ocean providing the heat required for mantle melting were at least locally present (Jolliff *et al.*, 2000a; Wiczorek and Phillips, 2000). The lateral and depth variation of crustal composition has been assessed from compositional mapping of central peaks (Wiczorek and Zuber, 2001) and ejecta blankets of large impact basins (Bussey and Spudis, 2000). Deeply excavated ejecta are found to be more mafic than the surface material (Pieters and Tompkins, 1999).

10.02.5.4 Lunar Crust

The circular maria are frequently associated with mass concentrations (mascon basins) causing a positive anomaly in the lunar gravity field due to the larger density of the basalt layer compared to that of the surrounding anorthositic crust. Uplift of the crust–mantle interface provides another contribution to the positive gravity anomaly. Some mascon basins are known that do not appear to be associated with mare volcanism (Konopliv *et al.*, 1998, 2001). Neumann *et al.* (1996) and Wiczorek and Phillips (1999) have suggested that the lunar mascons might

partly result from superisostatic uplift of the crust–mantle interface.

The dynamical range of the lunar topography varies between 5 and 6 km on the near side and 16 km on the far side due to the presence of the 2500-km diameter and 8-km deep South Pole Aitken basin (Zuber *et al.*, 1994). This ancient basin was formed by a huge impact that might have penetrated through the crust into the upper mantle thereby creating a low-albedo mafic anomaly. However, using five-color images obtained by the Clementine spacecraft, Pieters *et al.* (1997) argue that the mineralogy of the mafic component represents lower crust rather than upper-mantle material. Wieczorek and Phillips (1998) also suggest that there is still a 10–20-km-thick layer of crustal material present within the basin.

There is a pronounced dichotomy between the near-side and far-side crustal thickness as a consequence of the early differentiation of the Moon. Several factors such as variable heat transfer in the molten lunar interior and the large-scale insulation due to protocrust formation and thick impact ejecta may have contributed to the asymmetry (Jolliff *et al.*, 2000b). An early analysis of body-wave phases from artificial impacts of known impact time and location provided evidence for a dual-layered crust about 60 km thick beneath the Apollo 12 and 14 stations near Mare Cognitum (Toksöz *et al.*, 1974), whereas a putative thickness of 75 ± 5 km was derived from seismic data near the Apollo 16 highland site (Goins *et al.*, 1981). Previous estimates of the crustal thicknesses varied from 30–35 km under mascon basins to 90–110 km beneath the highlands, whereas irregular maria have intermediate thickness values of 50–60 km (Bills and Ferrari, 1977). From a re-analysis of gravity data acquired by the Apollo and Clementine spacecraft and assuming a thickness of 55 km at the Apollo 12/14 site, the thickness of the lunar farside crust has been estimated at 67 km. This would result in a mean thickness of 61 km if a uniform crustal composition is assumed (Neumann *et al.*, 1996).

A difference in crust thickness between near side and far side is thought to contribute substantially to the 1.7 km offset of the CoM relative to the center of figure CoF of the Moon in the direction of Earth (Kaula *et al.*, 1974; Hood and Jones, 1987; Zuber *et al.*, 1994). Wieczorek and Phillips (1998) have computed a variety of crustal thickness maps for the Moon, assuming both homogeneous and dual-layered crusts. The homogeneous crust model

characterized by a constant crustal density provides a total crust thickness of 66 km, whereas the preferred dual-layered model of the lunar crust consisting of a 31-km-thick upper crust and a 29-km-thick lower crust yields a total thickness of 60 km. The gravitational field measurements of the Lunar Prospector spacecraft suggest a mean crustal thickness of about 70 km assuming Airy compensation of the lunar highlands (Konopliv *et al.*, 1998) (*see* Chapter 10.05).

10.02.5.5 Lunar Seismology and Mineralogy

The Moon is the only planetary body other than the Earth for which a seismic velocity structure has been derived from analyses of the Apollo seismic data set (*see* Chapter 10.03). A seismic network of four stations on the lunar near side, installed at the landing sites of Apollo 12, 14, 15, and 16 from 1969 to 1972, continued to operate until it was turned off in September 1977. The seismic activity of the Moon is provided by deep moonquakes located at 850–1000 km depth, shallow moonquakes or high-frequency teleseismic events situated at 50–220 km depth, and meteoroid impacts onto the lunar surface. The deep moonquakes, apparently confined to the lunar near side, are most numerous and triggered by tidal deformation of the Moon. More than 12 000 events associated with 81 identified sources ('nests') have been recorded during the lifetime of the Apollo seismic network. It is likely that about 30 nests are located on the lunar far side. This implies that either the Moon's deep interior within about 40° from the sub-Earth antipode is nearly aseismic or, alternatively, that the region of the deep lunar interior deflects seismic waves and is highly attenuating for S waves, thereby impeding the localization of far side moonquake source regions (Nakamura, 2005).

Early seismic analyses were based on a limited set of arrival-time readings (Goins *et al.*, 1981), whereas the model of Nakamura (1983) employs the complete data set of 5-year simultaneous operation of four Apollo seismometers including more deep moonquake sources. More detailed lunar velocity and density structure models have been obtained from a new inversion of different subsets of the Apollo seismic data set by applying various inversion techniques to revised arrival-time readings (Khan *et al.*, 2000; Khan and Mosegaard, 2002; Khan *et al.*, 2004; Lognonné *et al.*, 2003; Chenet *et al.*, 2006).

The multilayer model of Goins *et al.* (1981) consists of a dual-layer crust, an upper mantle, an intermediate transition zone, and a lower mantle.

The crust is subdivided into a 20-km-thick upper layer with P-wave velocity $V_P = 5.1 \text{ km s}^{-1}$ and S-wave velocity $V_S = 2.96 \text{ km s}^{-1}$ and underlain by a lower-crust layer with $V_P = 6.8 \text{ km s}^{-1}$ and $V_S = 3.9 \text{ km s}^{-1}$ varying between 20 and 60 km in thickness. The upper mantle then extends from 60 to 400 km depth with average seismic velocities of $V_P = 7.7 \pm 0.15 \text{ km s}^{-1}$ and $V_S = 4.45 \pm 0.05 \text{ km s}^{-1}$. The moderate velocity decrease with depth is believed to be related to the temperature increase with depth. The corresponding seismic quality factors are $Q_P = 5000$ and $Q_S = 3000$, respectively. A narrow transition zone is situated between 400 and 480 km depth and reveals a prominent decrease of the shear-wave velocity, thereby creating a seismic shadow zone. The substantial decrease of the shear-wave velocity at the base of the transition zone has been interpreted in terms of a compositional change to a more primitive undifferentiated interior. The lower mantle ranges from 480 to 1100 km depth with average seismic velocities of $V_P = 7.6 \pm 0.6 \text{ km s}^{-1}$ and $V_S = 4.2 \pm 0.1 \text{ km s}^{-1}$ and corresponding seismic quality factors of $Q_P = 1500$ and $Q_S = 1000$, respectively. However, significant shear-wave attenuation accompanied by a Q_S drop by one order of magnitude occurs below a depth of 1100 km and suggests that the lowermost lunar mantle is at least partially molten.

The model of Nakamura (1983) includes a four-layer crustal structure that was introduced to satisfy the P-wave traveltimes of artificial impacts. The lunar mantle is subdivided into three layers with discontinuities at 270 and 500 km depth. The average velocities in the upper mantle above 270 km depth decrease from $V_P = 7.74 \text{ km s}^{-1}$ and $V_S = 4.49 \text{ km s}^{-1}$ to $V_P = 7.46 \text{ km s}^{-1}$ and $V_S = 4.25 \text{ km s}^{-1}$ between 270 and 500 km depth. In contrast to earlier studies based on a limited data set, the average velocities in the middle mantle between depths of 500 and 1000 km are about 8.26 and 4.65 km s^{-1} , respectively. The relatively high velocities in the middle mantle layer may represent Mg-rich olivine rock left over from early melting and differentiation of the deep lunar interior. The multilayer lunar interior model suggested by Nakamura (1983) is an approximation to more realistic continuous models with P and S velocities gradually decreasing with depth.

Contrary to previous studies, mean crustal thickness of only $45 \pm 5 \text{ km}$ (Khan *et al.*, 2000) or $38 \pm 3 \text{ km}$ (Khan and Mosegaard, 2002) have been proposed based on a re-analysis of Apollo lunar seismic data (Figure 7). The P-wave velocity increases from the

surface to the crust–mantle transition. The upper mantle extends from 45 to 500 km depth with average P- and S-wave velocities of $8.0 \pm 0.8 \text{ km s}^{-1}$ and $4.0 \pm 0.4 \text{ km s}^{-1}$, respectively. In contrast to the model of Nakamura (1983), the upper mantle is characterized by constant seismic velocities indicating a homogeneous structure and composition. Similar to the model of Nakamura (1983), the transition to the middle mantle at a depth of $560 \pm 15 \text{ km}$ is marked by a sharp increase to $V_P = 9.9 \pm 1.9 \text{ km s}^{-1}$ and $V_S = 5.9 \pm 0.9 \text{ km s}^{-1}$. It should be noted, however, that such high seismic velocities are difficult to reconcile with any known mineral phase assemblages. An intermediate low-velocity layer may cover the depth range from 620 to 700 km. Below that depth, extends a high-velocity layer with P- and S-wave velocities of 11.0 ± 2.1 and $6.0 \pm 0.7 \text{ km s}^{-1}$, respectively, encompassing the deep moonquake source region.

Using arrival-time readings of about 60 deep and shallow lunar quakes and meteoroid impacts, Lognonné *et al.* (2003) propose crust thicknesses in the range $30 \pm 2.5 \text{ km}$ at the Apollo 12/14 site situated in the Procellarum-KREEP-Terrain. The corresponding temperature range of the underlying pyroxenite-rich mantle compares well to electrical conductivity profiles retrieved from early Apollo orbiter observations (Khan *et al.*, 2006b). The mantle temperatures are still sufficient to keep an Fe–FeS core molten but not a pure iron core. Chenet *et al.* (2006) limit themselves to a seismic analysis of seven artificial and 19 natural usable meteoroid impacts suggesting only moderate lateral variations in lunar near-side crust thickness. The crust thickness beneath the Apollo 12, 14, 15, and 16 landing sites is found to be 33 ± 5 , 31 ± 7 , 35 ± 8 , and $38 \pm 7 \text{ km}$, respectively, consistent with a combined gravity/topography analysis. Considering a mean crust density and an upper mantle P-wave velocity of $\rho = 2900 \text{ kg m}^{-3}$ and $V_P = 7.57 \text{ km s}^{-1}$, respectively, the lunar anorthositic crust would be much thinner than previously thought with a mean thickness of only $40 \pm 5 \text{ km}$ (Chenet *et al.*, 2006). Assuming an anorthositic composition for the 40-km-thick crust, Lognonné *et al.* (2003) find the Moon's silicate portion (mantle + crust) to be composed of 53.5 wt.% SiO_2 , 6.4 wt.% Al_2O_3 , 13.3 wt.% FeO , 21.9 wt.% MgO , and 4.9 wt.% CaO with a bulk uranium content of 28 ppb.

The most prominent increase in seismic velocity that occurs at a depth of $\sim 500 \text{ km}$ represents the transition from the upper mantle to the middle mantle. This discontinuity has been interpreted in terms of a mineralogic phase transition from the spinel to

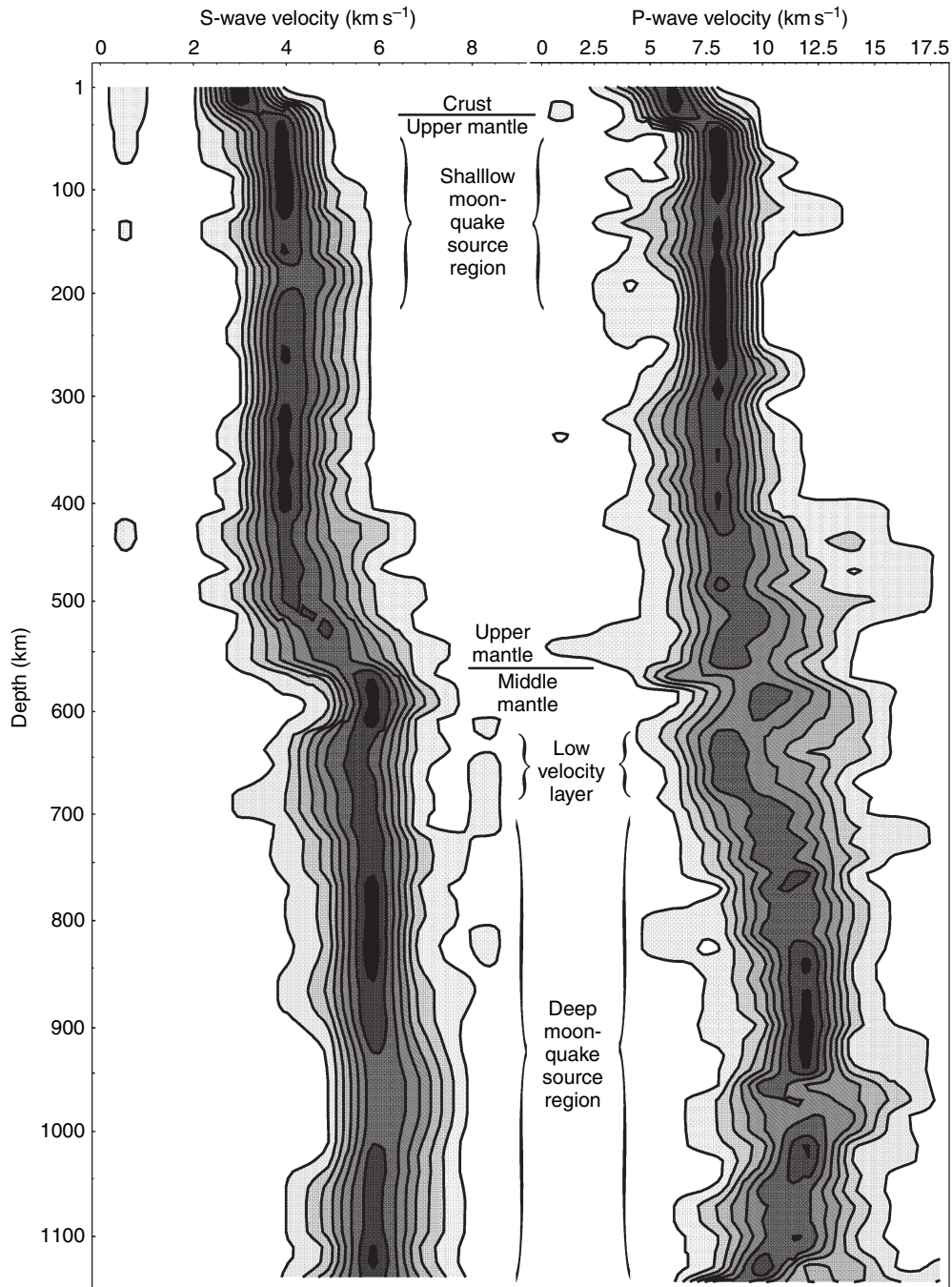


Figure 7 Marginal posterior probability distributions illustrating the range of possible (left) S-wave and (right) P-wave velocity structures of the Moon based on a total number of 50 000 models. The contour lines define nine equally sized probability density intervals for the distributions. Note that maximum probability does not necessarily correspond to maximum likelihood of a calculated velocity structure. Adapted from Khan A and Mosegaard K (2002) An inquiry into the lunar interior: A nonlinear inversion of the Apollo lunar seismic data. *Journal of Geophysical Research* 107(E6): 50036 (doi:10.1029/2001JE001658).

the garnet stability field. Alternatively, a change in composition to more aluminous and MgO-rich mafic silicates has been invoked thereby increasing the Mg

number below this depth (Nakamura, 1983; Khan *et al.*, 2006a). The re-analysis of the Apollo lunar seismic data indicates a homogeneous, constant-

velocity upper mantle extending down to 560 ± 15 km depth, whereas the radial velocity distribution suggests more inhomogeneous middle- and lower-mantle layering (Khan *et al.*, 2000; Khan and Mosegaard, 2002). The compositional change across the discontinuity together with the homogeneity of the upper mantle and the inhomogeneity of the middle mantle has been interpreted in terms of the initial depth of melting and differentiation during the magma-ocean phase of the Moon (Hood and Zuber, 2000). Based on mare-basalt petrology and thermal evolution considerations, Elkins-Tanton *et al.* (2003a) identify the 500-km discontinuity with the maximum depth of melting beneath the Procellarum-KREEP-terranes on the lunar near side. It is also possible that the 500-km discontinuity represents stratified olivine- and orthopyroxene-rich cumulates that were subsequently emplaced at the bottom of the lunar magma ocean. The mineralogical layering is supported by seismic inversions that account for thermodynamic mineral phase equilibria (Kuskov and Fabrichnaya, 1995; Kuskov, 1995, 1997; Kuskov and Kronrod, 1998).

The existence of a small lunar core could not be confirmed or rejected solely on the basis of the seismic data acquired by the Apollo missions. During the limited operational period of the lunar seismic network with stations on the near-Earth hemisphere, only one meteoroid event was detected with seismic rays crossing a central low-velocity zone from which the size of a lunar core was estimated for the first time. However, Sellers (1992) has shown that a relocation of this meteorite impact on day 263 in 1973 can explain the arrival-time and signal-amplitude data without requiring the presence of a lunar core. From tentative arrival-time determinations of two of the largest, most distant impacts it has been found that the corresponding seismic phases could have traveled at a P-wave velocity of about 5 km s^{-1} through a lunar core about 400–450 km in radius (Sellers, 1992). Considering the ambiguity inherent in the Apollo lunar seismic data, first reliable recordings of seismic phases traveling through the central region of the Moon are therefore expected from future measurements, like those once envisaged for the Japanese Lunar-A mission (Mizutani 1995).

10.02.6 Mercury

The planet Mercury is the least well-known body among the terrestrial planets and is unique in many respects. It represents an end member of the

terrestrial planets with respect to its density and distance from the Sun and thereby provides important constraints on planetary formation and evolution in the innermost part of the solar nebula (Balogh and Giampieri, 2002; Solomon, 2003).

10.02.6.1 General

Mercury is 4878 km in diameter, roughly one-third the size of Earth, and occupies only about 6% of the volume of Earth. Albeit substantially smaller in size, Mercury's surface gravity of 3.7 m s^{-2} is like that of the larger planet Mars. In 1974 and 1975, the Mariner 10 spacecraft provided the first close-up look of the planet during three encounters. From these flybys, better values of the planet's mass, mean radius, and average density were obtained. Less than half of the surface was covered by images at an average resolution of 1 km, and less than 1% at 100–500 m resolution, resulting in a limited characterization of surface morphology and geological evolution. Among the most important findings of the Mariner 10 spacecraft was the then unexpected detection of a magnetic field of internal origin (Ness, 1979).

The densely cratered surface of Mercury suggests that it is one of the oldest surfaces in the solar system, but not necessarily older than the lunar and Martian highlands. About 60% of the known surface is covered by intercrater and smooth plains possibly caused by volcanic emplacement. Based on the notion that the Mercurian plains closely resemble the lunar light plains, they might also be formed of impact materials, perhaps impact melt or other basin ejecta that behaved more like a fluid when emplaced (Wilhelms, 1976). Lobate scarps and widespread volcanic plains suggest an early evolution in which volcanically induced expansion preceded a phase of planetary contraction (Solomon, 2003).

Mercury's orbit about the Sun has a semimajor axis of 0.387 AU, an eccentricity of 0.206, and an inclination of 7° relative to the ecliptic. Therefore, the orbital distance from the Sun varies between 0.308 AU at perihelion and 0.466 AU at aphelion in the course of one revolution, causing significant tidal distortion of the planet (Burns, 1976; Van Hoolst and Jacobs, 2003). Furthermore, the near-surface layer of Mercury is exposed to a severe thermal environment in terms of elevated surface temperatures and high subsurface temperature gradients due to the planet's proximity to the Sun with an insolation of up to 15 kW m^{-2} . Related diurnal surface temperature variations between 90 and 740 K are greater than on

any other planet or satellite in the solar system (Strom, 1997). Radar observations from the Earth have shown that the rotation period (58.6 d) is locked into a 3:2 resonance with the orbital period (87.7 d). As a consequence of the 3:2 spin–orbit coupling caused by tidal interactions with the Sun, one solar day on Mercury lasts 176 Earth days and corresponds to two revolutions or three rotations of the planet. While the distribution of solar irradiation is symmetric between both hemispheres, the significant orbital eccentricity causes longitudinal variations superimposed on the latitudinal variation of the solar irradiation (Van Hemelrijck and Vercheval, 1981). Due to the lack of a substantial atmosphere, the surface of Mercury has been heavily cratered and fragmented by impacts and small-particle bombardment resulting in a planet-wide, fine-grained, and thermally insulating regolith layer (Langevin, 1997). The thermal and electrical properties of the Mercurian regolith derived from Mariner 10 measurements are similar to those of the Moon (Chase *et al.*, 1976). Even large-amplitude surface temperature perturbations are thus expected to rapidly fade away with depth and will be negligible below several thermal skin depths (Vasavada *et al.*, 1999; Hale and Hapke, 2002).

10.02.6.2 Interior Structure

The large average density of $5430 \pm 10 \text{ kg m}^{-3}$ (Anderson *et al.*, 1987) is comparable to that of the Earth and Venus but much larger than that of the Moon and Mars. The corresponding zero-pressure density of about 5300 kg m^{-3} is even much higher than the uncompressed densities of Earth, Venus, and Mars which are about 4100, 4000, and 3800 kg m^{-3} , respectively. This suggests that Mercury contains a larger proportion of heavier elements such as iron than any other terrestrial planet. The mass concentration of iron should be about twice that in the Earth (Wasson, 1988). The existence of the weak intrinsic magnetic field and compressional surface features observed by Mariner 10 together with the large average density suggest that most of the iron is concentrated in a substantial Fe-rich core with a radius of roughly 0.8 times the planet radius (Figure 8). The core occupies about 42% of the planet's volume corresponding to a core mass fraction of two-thirds relative to the planet's mass or about twice that of the Earth (Siegfried and Solomon, 1974). If Mercury formed by the accretion of high-temperature condensates close to the Sun then a substantial depletion of volatiles such as sulfur should have occurred. This would translate into a refractory

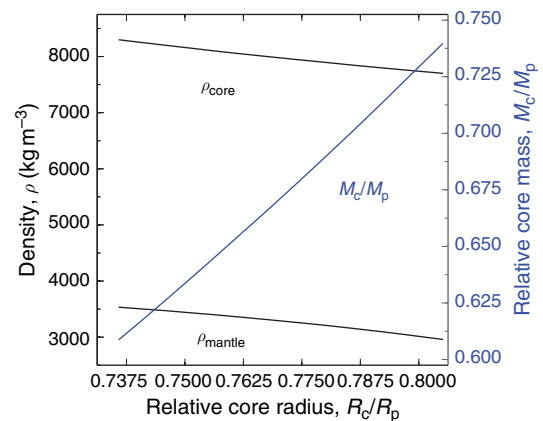


Figure 8 Two-layer model determinations of mantle and core density and core mass fraction M_c/M_p of Mercury vs relative core radius R_c/R_p based on a Mol factor of 0.3359. The core size of Mercury could be relatively well determined if the planet's moment of inertia becomes known.

bulk composition and a metallic core predominantly composed of iron with only small amounts of sulfur (Lewis, 1988; Goettel, 1988).

Radar ranging data suggest that the equatorial shape of Mercury is highly elliptical. However, since Mercury has not attained an equilibrium figure, its shape and gravitational field cannot be used to infer the size of its metallic core. There is a significant equatorial ellipticity $(a - b)/a = (540 \pm 54) \times 10^{-6}$. The CoF is offset from the CoM by $640 \pm 78 \text{ m}$ in the direction of the still unseen hemisphere of Mercury (Anderson *et al.*, 1996). The CoF–CoM offsets of all the terrestrial planets are plausibly attributed to hemispheric asymmetries in crustal thickness depending on the contrast $(\rho_m - \rho_s)/\rho_m$ between the densities of the mantle and the crust ρ_m and ρ_s , respectively. The magnitude of the CoF–CoM offset implies an excess crustal thickness of $<12 \text{ km}$, which is comparable to that obtained for the Moon. From a comparison between the equatorial shape and the gravitational equatorial ellipticity $C_{2,2}$ as inferred from the Mariner 10 flybys, Anderson *et al.* (1996) have concluded that the Mercurian crust could be $200 \pm 100 \text{ km}$ thick if Mercury's equatorial ellipticity were entirely compensated by Airy isostasy. Even the lower bound of 100 km is more than twice as large as the crustal thickness of the other terrestrial planets and the Moon and, therefore, difficult to reconcile with the planet's magmatic history if the Mercurian crust formed from volcanic emplacement of partial melts extracted from the underlying mantle.

10.02.6.3 Composition

Models of the interior structure rely on the mass and mean radius of the planet since a value for the moment-of-inertia factor is not available at present. A determination of the MoI factor, as envisioned by future missions to Mercury, would help distinguish an iron core from a more homogeneous distribution of iron in oxidized form within the planet (Schubert *et al.*, 1988). The spectral characteristics and high albedo of the surface of Mercury are consistent with the existence of a metal-poor and possibly highly differentiated, feldspathic crust that contains less FeO and TiO₂ (~2–4%) than the lunar highland crust (>15%) (Sprague *et al.*, 1994; Blewett *et al.*, 1997; Warell and Blewett 2004). This is taken as evidence for the strong internal differentiation of the planet and implies the former existence of a magma ocean (Jeanloz *et al.*, 1995). Additional assumptions about the chemistry and densities of a basaltic crust, a more primitive mantle, and an iron-rich core are then required to construct models of the interior in accordance with the mass and mean density of the planet. Possible interior structure models have been calculated for various bulk chemical compositions based on different condensation and accretion scenarios (e.g., Wood *et al.*, 1981). Accounting for pressure-induced compression and thermal expansion effects, Siegfried and Solomon (1974) and Harder and Schubert (2001) propose MoI factors in the range from 0.325 for fully differentiated models to 0.394 for chemically homogeneous, undifferentiated models. The silicate shell comprising crust and mantle layers is then 500–700 km thick. There is little variation of pressure, temperature, density, and elastic moduli with depth through the silicate shell (Figure 9). Density discontinuities induced by major phase transitions should not be present in the mantle due to small pressure increase with depth resulting in a pressure at the core–mantle boundary of about 7 GPa (Siegfried and Solomon, 1974; Harder and Schubert, 2001). If a crust layer were added with thickness and density of 50 km and 3000 kg m^{−3}, respectively, the radius of a large iron core would be about 1800–1900 km thereby corresponding to a MoI factor of about 0.34 (Figure 10). It is possible, however, that compositional changes occur across the mantle. Thermal history calculations show that an asthenosphere in the upper mantle may be sustained up to the present time (Conzelmann, 1994). This has important consequences for the magmatic history of the planet.

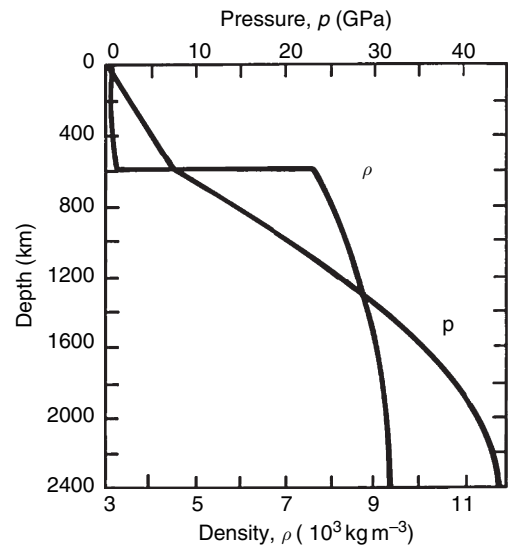


Figure 9 Variation of pressure p and density ρ versus depth for a fully differentiated model of Mercury's interior. Note that a refractory bulk composition is assumed (Schubert *et al.*, 1988). Adapted from Siegfried RW and Solomon SC (1974) Mercury: Internal structure and thermal evolution. *Icarus* 23: 192–205.

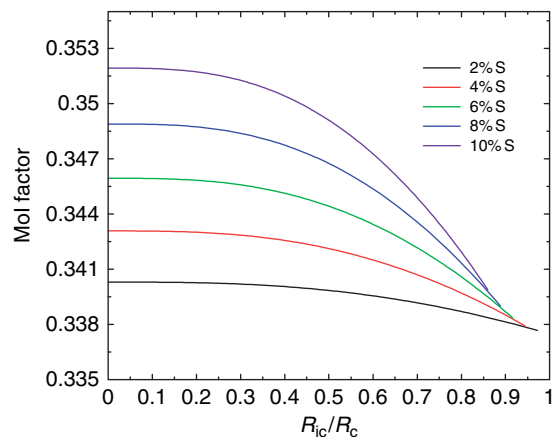


Figure 10 Mean MoI factor of a three-layer model of Mercury as a function of inner-core radius R_{ic} and core chemistry. R_{ic} is given relative to the radius of the core R_c .

10.02.6.4 Magnetic Field

Mercury is the only terrestrial planet other than the Earth with a perceptible dipole magnetic field. The presence of an internally generated magnetic field suggests that the iron core is at least partially liquid with an electrically conducting outer core of unknown thickness surrounding a solid inner core. Thermal evolution models indicate that the core

would have solidified early in the history of Mercury unless a light alloying element such as sulfur were present. A small amount of sulfur as suggested by [Stevenson *et al.* \(1983\)](#) is sufficient to depress the freezing point of a core alloy and is consistent with the refractory bulk composition as derived from the planet's condensation and accretion in the hot innermost part of the solar nebula. The freezing of an inner pure iron core would be accompanied by the enrichment of sulfur in the outer core thereby increasing the depression of the freezing point and maintaining a liquid outer-core shell in spite of planet cooling ([Figure 11](#)). Thermal history models taking into account parametrized convective heat transport through the mantle indicate sulfur concentrations of 1–5 wt.% to retain a liquid outer core shell at the present time ([Stevenson *et al.*, 1983](#); [Schubert *et al.*, 1988](#); [Spohn, 1991](#)). Based on parametrized models of the coupled thermal, magmatic, and tectonic evolution of Mercury, [Hauck *et al.* \(2004\)](#) conclude that a dry-olivine mantle rheology, thorium-dominated radiogenic heating suggesting late silicate-mantle vaporization ([Cameron *et al.*, 1988](#)), and a bulk core sulfur content of at least 6.5 wt.% is needed to explain both the planet's radial contraction of 1–2 km and the presence of a dynamo-driven, intrinsic magnetic field. Models of mantle convection including pressure and temperature-dependent rheology demonstrate that the cooling history of a terrestrial planet is governed by the growth of its lithosphere while the deep interior remains relatively hot. These models compare well to the parametrized convection

calculations but produce thicker outer core shells at identical sulfur concentrations. Depending on the stiffness of the mantle rheology, a liquid outer-core layer is then sustained even for sulfur concentrations as small as 0.2 wt.% consistent with cosmochemical arguments in favor of a volatile-poor planet ([Conzelmann, 1994](#); [Spohn *et al.*, 2001b](#)). The 2-km radial contraction of Mercury in the absence of large-scale magmatism about 4 Gyr ago may be linked to core shrinkage due to solid-inner-core growth and mantle cooling governed by lithospheric thickening and sluggish mantle convection ([Schubert *et al.* 1988](#)).

10.02.6.5 Future Exploration

Future spacecraft missions together with Earth-based radar observations are expected to provide important new constraints on the internal structure of Mercury by determining its gravity field, large-scale topography, and tidal and rotational parameters with unprecedented accuracy. The ratio C_m/C between the axial moment of inertia of the planet's solid portion and that of the entire planet depends on the coupling between core and mantle and provides clues to the physical state of the outermost part of Mercury's core. C_m/C will be around 0.5 for a liquid core or liquid outer-core shell ([Figure 12](#)) and about 1 in case of a solid core. C_m/C can be obtained from accurate measurements of the planet's 88-day forced libration amplitude in longitude, the obliquity, and the second-degree coefficients C_{20} and C_{22} of the spherical harmonic expansion of the planet's

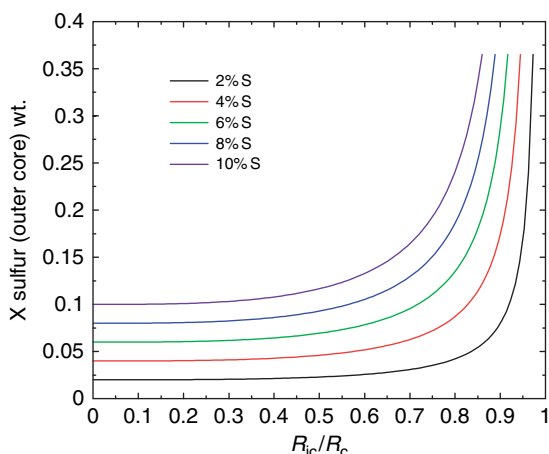


Figure 11 Sulfur content of the outer core of a three-layer model of Mercury as a function of inner core radius R_{ic} and core chemistry. R_{ic} is given relative to the radius of the core R_c .

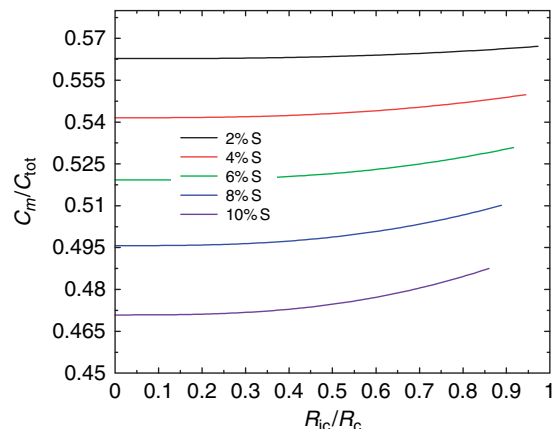


Figure 12 Ratio between the axial moment of inertia of Mercury's solid portion and that of the entire planet as a function of inner core radius R_{ic} and core chemistry. R_{ic} is given relative to the radius of the core R_c .

gravitational field (Peale, 1976, 1988) (see Chapter 10.04). C and C_m/C will permit calculation of the inner-core radius r_i and the outer core density for prescribed silicate mantle and solid-inner-core densities. Since Mercury is tidally flexed in its highly eccentric orbit about the Sun, the tidal Love number k_2 can be derived from time-variable gravitational field measurements on a spacecraft orbiting the planet (Van Hoolst and Jacobs, 2003). k_2 may provide useful constraints on the radial rigidity distribution and the extent of core differentiation for significant inner-core sizes, that is, $R_i/R_c > 0.5$ (Figure 13). Furthermore, the higher-order components of the gravitational field can be used to estimate crust thickness variations at short wavelengths and core–mantle boundary undulations at long wavelengths; the latter should be easily detectable due to the large size of Mercury’s core relative to the planet’s size (Spohn *et al.*, 2001b).

No seismic data for Mercury exist. However, the periodic deformation of Mercury by solar tides may have important consequences for the planet’s seismic environment. Due to its highly elliptic orbit about the sun and its bound rotation, Mercury is exposed to strong tidal forces (Van Hoolst and Jacobs, 2003). As a result, the seismic environment of Mercury may feature large numbers of lunar-like quakes.

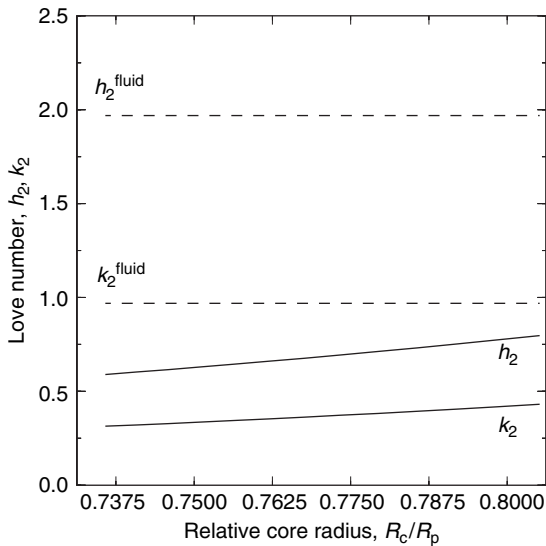


Figure 13 Tidal potential Love number k_2 of Mercury as a function of core radius R_c relative to the planet’s radius R_p . A two-layer structural model with a solid mantle and a fluid core is assumed. The fluid Love numbers k_2^{fluid} and h_2^{fluid} are related to the Mol factor fixed at a value of 0.3359 in these models.

10.02.7 Mars

The size of Mars is about half the size of the Earth and its mass is about one-tenth the mass of the Earth. The uncompressed density of roughly 3800 kg m^{-3} is significantly lower than the uncompressed densities of the Earth and Venus. The environmental conditions are the most earthlike among the terrestrial planets with surface temperatures varying between 140 K at night in winter and 300 K at midday in summer. Mars is thought to be a one-plate planet, as are the Moon and Mercury, lacking plate tectonics at least at the present time.

10.02.7.1 General

The Martian surface is characterized by the hemispheric dichotomy between relatively sparsely cratered lowland plains in the north and the heavily cratered southern highland terrain once subjected to the post-accretional heavy bombardment of the inner solar system. The Tharsis rise is situated close to the near-equatorial boundary between the Northern and Southern Hemispheres and represents a giant volcanic dome established early in the planet’s history. Major volcanoes such as Olympus Mons and the Tharsis Montes were emplaced on top of the Tharsis rise. The magmatic evolution of the planet is characterized by a progressive concentration of the volcanic activity to the Tharsis area and, to a lesser extent, to the Elysium area located about 100° to the west in the northern lowland plains. The morphology of the boundary between the two hemispheres is dominated by outflow channels and chaotic terrain extending along broad gradual slopes rather than several-kilometer-high escarpments. Some portions of the dichotomy boundary are composed of fretted terrane and others are sculptured by scarps (Smith and Zuber, 1996). For review articles on the geophysics and evolution of Mars, we refer the reader to Schubert *et al.* (1992), Spohn *et al.* (1998, 2001a), and Solomon *et al.* (2005).

10.02.7.2 Interior Structure

The global topography and gravitational field of Mars have been determined with high accuracy using laser altimetry and two-way Doppler tracking of the Mars Global Surveyor (MGS) spacecraft (Smith *et al.*, 1999b,a; Zuber *et al.*, 2000; Lemoine *et al.*, 2001). Further improvements of the gravity

model of Mars have been achieved by combining MGS tracking data with Mars Odyssey tracking data and surface tracking data from the Pathfinder and Viking 1 landers; the latter permits improvement of the parameters describing the orientation of the planet's rotational axis (Konopliv *et al.*, 2006). The rotational flattening of Mars results in a difference between the polar (north–south average) and equatorial radii of about 20 km (Seidelmann *et al.*, 2002). The variation of topography with respect to the Martian geoid is about 30 km, representing the largest dynamic range of any terrestrial planet. The hemispheric dichotomy of Mars is related to an offset of about 3 km between the planet's CoM and CoF along the polar axis. The Tharsis Bulge causes an additional offset of about 1.4 km along an equatorial axis in the direction of Tharsis. The topographic data show that the Tharsis rise consists of two broad rises, a larger, nearly circular southern rise superposed on the highlands that contains the Tharsis volcanoes and a smaller northern rise superposed on the lowlands that contains the shield volcano Alba Patera (Smith *et al.*, 1999a).

Whereas the gravitational field of the elevated Southern Hemisphere is relatively featureless and implies a state of near-isostatic compensation, the northern lowland plains reveal a wider range of gravitational anomalies (Smith *et al.*, 1999b). The dichotomy boundary is not clearly resolved on the gravity map, whereas the Tharsis Montes, Olympus Mons, Valles Marineris, and Isidis impact basin are visible as individual gravitational anomalies in the aeroid. Major gravity highs are associated with the Tharsis and Elysium volcanoes indicating that they are not isostatically compensated. Large impact basins reveal negative annular anomalies with a central positive anomaly. The global crust and upper mantle structure of Mars has been derived from MGS measurements of gravity and topography. The Bouguer gravity has been interpreted in terms of crustal thickness variations. In these models the thickness of the Southern Hemisphere crust decreases progressively from south to north, whereas the northern lowlands are characterized by a more uniform crust thickness (Zuber *et al.*, 2000; Neumann *et al.*, 2004).

Because of the nonuniqueness inherent in the interpretation of gravitational field data, unless they can be tied to direct seismic measurements, the mean density and thickness of the Martian crust are unknown at present. Plausible Martian crust densities range from 2700 to 3100 kg m⁻³ (Wieczorek and

Zuber, 2004) based on end-member-type compositional models of the Martian crust. The lower estimate of about 2700 kg m⁻³ represents an andesitic–basaltic composition obtained from Pathfinder–APXS measurements of soil-free Martian rocks (Brückner *et al.*, 2003). The upper estimate of about 3100 kg m⁻³ represents porous basaltic shergottites (Britt and Consolmagno, 2003) believed to be samples of the Martian crust released during one or several giant impacts (McSween, 1994). These rocks are further believed to represent end members of the composition of well-mixed Martian soil on a planetary scale (Nimmo and Tanaka, 2005). Using a spectral localization method to analyze volcanic surface loads, Belleguic *et al.* (2005) have reported considerably higher crustal densities beneath the Elysium rise of 3270 ± 150 kg m⁻³, whereas the load densities related to the major Martian volcanoes except Alba Patera are best constrained by a value of 3200 ± 100 kg m⁻³. The latter density is similar to that of Shergotty-type basaltic meteorites thought to have originated from Mars. This implies that the Martian lowland crust is composed of more mafic constituents than the southern highland crust and that the hemispheric difference in elevation may be mainly attributed to a Pratt-like isostatic compensation mechanism (Belleguic *et al.*, 2005). Present estimates of the mean crustal thickness of Mars are entirely based on indirect geophysical studies like local relationships between gravity and topography and/or geochemical arguments and may range between 30 and 80 km (Neumann *et al.*, 2004; Wieczorek and Zuber, 2004; Solomon *et al.*, 2005) although crust thicknesses of up to about 100 km are consistent with global geophysical constraints (Sohl and Spohn, 1997; Kavner *et al.*, 2001; Gudkova and Zharkov, 2004; Sohl *et al.*, 2005). Assuming a Bouguer reduction density of 2900 kg m⁻³ and a crust–mantle density contrast of 600 kg m⁻³, crust thicknesses vary from about 6 to 102 km, the former of which is located beneath the center of Isidis and the northwestern floor of Hellas Planitia (Neumann *et al.*, 2004). Larger crust thickness might be unlikely, however, since ductile flow in the warm lower crust could cause relaxation of lateral crustal thickness variations (Zuber *et al.*, 2000; Zuber, 2001; Nimmo and Stevenson, 2001). The crust thickness could be further limited by the pressure-induced transition from basalt to eclogite that may occur in the lower Martian crust (Babeyko and Zharkov, 2000).

Vector magnetic field observations, obtained at altitudes between about 100 and 200 km subsequent

to orbit insertion of the Mars Global Surveyor spacecraft, have been compiled into a global magnetic field map of the Martian crust (Connerney *et al.* 2005). Although Mars lacks an intrinsic magnetic field at present, the Martian crust acquired intense magnetization in the past, hinting at the existence of a strong internally generated field at that time. Crustal remanent magnetization has been found to exceed that of Earth by more than an order of magnitude and is mainly confined to the most ancient, heavily cratered southern highland terrain (Acuña *et al.*, 1999; Connerney *et al.*, 1999). Linear magnetic features of up to 2000 km in length are frequently oriented in the east-west direction, some resembling a pattern of band-like features of alternating magnetic polarity (Connerney *et al.*, 2001). The Martian crust may have been magnetized during a time span of only a few hundred million years after planet formation when an active core dynamo driven by thermal convection produced an intense global magnetic field. If crust magnetization occurred later in the planet's evolution, a core dynamo driven by chemical convection associated with inner-core growth would be more likely (Connerney *et al.*, 2004). The lack of crustal magnetization in the vicinity of large impact basins (Hellas, Argyre, Isidis) is commonly attributed to cessation of the core dynamo when these basins formed about 4 Gyr ago during the Noachian period and demagnetized underlying crust layers (Acuña *et al.*, 1999). Alternatively, however, impact basin formation may predate the onset of the Martian core dynamo so that the magnetization of the southern highland terrain was caused by localized heating events followed by rapid cooling below the Curie temperature (Schubert *et al.*, 2000). The almost complete demagnetization of the Tharsis rise and other volcanic features implies that thermoremanent magnetization on Mars is confined to a relatively thin layer less than a few tens of kilometers thick. In a similar way, a possible former magnetization of the northern lowland crust may have been entirely erased by catastrophic volcanic flooding during the Hesperian period (Head *et al.*, 2002). Connerney *et al.* (2005) argue that variations in the crustal magnetic field can be associated with major geologic and topographic features, sometimes reminiscent of transform faults in oceanic crust on Earth. It is speculated that arcuate and linear magnetic features, similar to but much larger than those observed near mid-ocean ridges on Earth, could imply that early Noachian crust formation on Mars was accompanied by plate tectonics associated with crustal spreading in the

presence of a reversing dynamo (Connerney *et al.*, 2005).

Early attempts at modeling the deep interior structure of Mars suffered from poorly known values of its radius and moment of inertia. Improved measurements of the planet's mass M_p , radius r_p , gravitational potential and rotation rate by the Mariner, Viking, and Pathfinder spacecraft provided geodetic constraints required for models of the interior structure. The polar moment of inertia of Mars has been derived from a combined analysis of Mars Global Surveyor tracking and Mars Pathfinder and Viking Lander range and Doppler data. The reanalysis of the entire data set resulted in the most recent value of $C/M_p R_p^2 = 0.3650 \pm 0.0012$ (Yoder *et al.*, 2003), lower than the previously accepted value of $C/M_p R_p^2 = 0.3662 \pm 0.0017$ (Folkner *et al.*, 1997). The improved value is consistent with the model of a mostly hydrostatic planet with a non-hydrostatic contribution to the MoI factor entirely related to the axisymmetric distribution of topographic loads about Tharsis (Kaula, 1979). Using the improved value of $C/M_p R_p^2$ and taking into account the planet's gravitational oblateness and minor contributions due to the Tharsis rise results in a mean MoI factor of $I/M_p R_p^2 = 0.3635 \pm 0.0012$ and suggests a stronger concentration of mass toward the center than previously thought, with consequences for the planet's bulk chemistry and interior structure (Sohl *et al.*, 2005). As a consequence of the improved lower MoI factor, the Martian mantle may be less dense, about several tens of kg m^{-3} , with a smaller iron content than previously thought if crust thickness and core size are specified. It further implies that the Martian crust is several tens of kilometers thicker than previously thought if crust and mantle densities and core size are given. Finally, it suggests several tens of kilometers larger core radii if other parameters like core density, crust density, and crust thickness are fixed (Figure 14). If the crust thickness increases, dense mantle material will be replaced by less-dense crust material thereby reducing the planet's MoI factor. The mass deficit that arises cannot be compensated simply by increasing the core density, since this would even further reduce the MoI factor for a given core size. Therefore, to account for both the planet's mean density and mean MoI factor at constant core size, the mantle density will be required to increase and core density simultaneously to decrease. In terms of composition, the presence of a thicker crust requires the silicate mantle to be more enriched in iron with an increasing amount of light

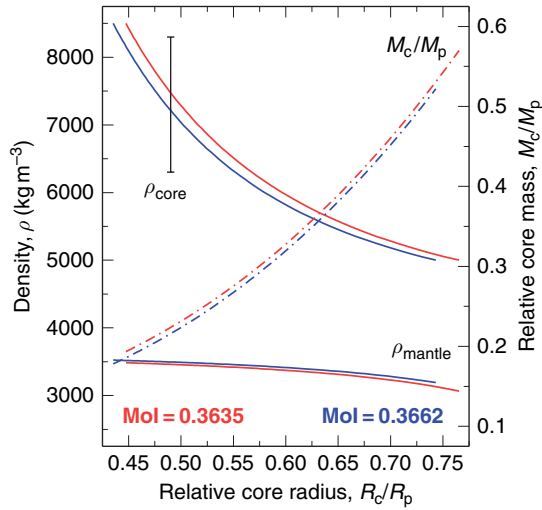


Figure 14 Two-layer model determinations of mantle and core density and core mass fraction M_c/M_p of Mars vs relative core radius R_c/R_p based on a Mol factor of 0.3635 (red) and 0.3662 (blue), respectively. Martian core densities are thought to range between those of γ -iron and iron sulfide as indicated by the error bar. Adapted from Sohl F, Schubert G, and Spohn T (2005). Geophysical constraints on the composition and structure of the Martian interior. *Journal of Geophysical Research* 110: E12008 (doi:10.1029/2005JE002520).

alloying elements such as sulfur concentrated in the core. Additionally, the contribution of a thicker crust to the planet's bulk composition will become more pronounced (Figure 15).

The determination of the solar tidal potential Love number $k_2 = 0.153 \pm 0.017$, based on the analysis of 3 years of Mars Global Surveyor radio tracking data, indicates that the planet's interior is still sufficiently hot that at least the outer part of the Martian core is liquid (Yoder *et al.*, 2003). The reliable determination of the planet's tidal potential Love number will steadily improve as further spacecraft radio tracking data are collected, thereby additionally constraining the size of the Martian core. A small apparent tidal lag angle γ of about 0.7° has been obtained from a combined analysis of Viking and Mars Global Surveyor observations of Phobos' orbital position (Bills *et al.*, 2005). The corresponding estimate of Mars's tidal quality factor $Q_p = 1/\tan \gamma \approx 85$ is within the range of former estimates of $Q_p = (100 \pm 50)$ (Smith and Born, 1976; Yoder, 1982). It has been shown previously that inelastic contributions to k_2 amount to only 1% of that caused by the planet's elastic tidal response if $Q_p \approx 100$ is assumed (Sohl and Spohn, 1997).

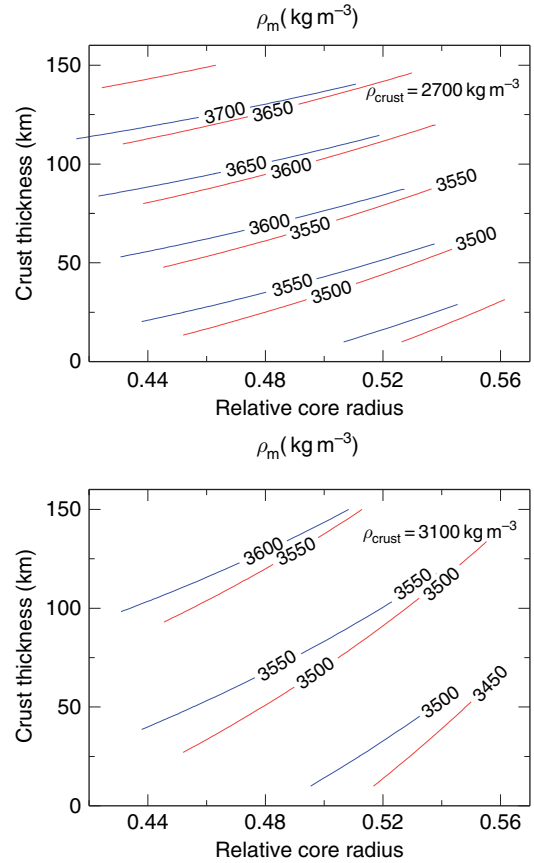


Figure 15 Contours of mantle density ρ_m as a function of relative core radius R_c/R_p and crust thickness based on a Mol factor of 0.3635 (red) and 0.3662 (blue), respectively. Mean crystal density is fixed at (top) 2700 and (bottom) 3100 kg m^{-3} . Adapted from Sohl F, Schubert G, and Spohn T (2005). Geophysical constraints on the composition and structure of the Martian interior. *Journal of Geophysical Research* 110: E12008 (doi:10.1029/2005JE002520).

10.02.7.3 Composition

Considerations of element correlations in SNC meteorites and cosmochemical constraints suggest that Mars was formed by the homogeneous accretion of two geochemically distinct components, a highly reduced refractory component and a volatile-rich one. In this model, the former did not include elements more volatile than sodium or potassium, however, it contained all other elements in the same abundance ratios as in primitive carbonaceous chondrites of class CI. Iron and all siderophile elements are in the metallic state, and even silicon is partially metallic. This material existed mainly in the feeding zone of the growing Earth (Dreibus and Wänke, 1985; Wänke and Dreibus, 1988). In this

model, Mars is differentiated into a FeO-rich silicate mantle containing radiogenic heat sources in terrestrial abundances and a sulfur-rich Fe-Ni-FeS core of about 22% of the planet's mass containing about 14 wt.% sulfur with a radius roughly 50% of the surface radius. Longhi *et al.* (1992) have recast the mantle composition of Dreibus and Wänke (1985) into a pressure-dependent mineralogy resulting in an upper olivine-rich part, a transition zone composed of silicate-spinel, and a lower perovskite-rich layer. The model provides a mean dimensionless MoI factor of 0.353 and is consistent with the geochemical constraint of a bulk Fe/Si ratio of 1.71 representative of the composition of CI carbonaceous chondrites. From models that use identical sets of material parameter values for crust, mantle, and core, as derived from geochemical analyses of SNC meteorites, and that take into account self-compression and thermal expansion of the Martian interior, it has been concluded that it is impossible to reconcile the assumption of a bulk planet CI Fe/Si ratio with the observed value of the polar moment-of-inertia factor (Sohl and Spohn, 1997).

The Martian core is sufficiently large that even small changes in core size will result in significant changes of core volume. Since the core contributes most of the iron, a significant change in core volume can be expected to result in a notable modification of the bulk planet Fe/Si ratio. Modifications of the Fe/Si ratio due to changes in core volume may be partly compensated, however, by variable mantle iron contents in combination with crust thickness variations because of the significant mass fraction of the planet's silicate portion. The bulk-planet Fe/Si ratio is also notably dependent on the thermal state of the core because of the temperature dependence of the EOS parameters of iron and iron sulfide as the main core constituents (Fei *et al.*, 1995; Kavner *et al.*, 2001). In Figure 16, radially symmetric density models of the Martian interior are compared for variable sulfur content of the core. The sulfur contents of the Martian core is unknown, but geochemical models predict a sulfur-rich core (McSween, 1994). Furthermore, light constituents such as iron hydrite may also be present in the core depending on the amount of hydrogen dissolved in the core alloy when subject to the pressure and temperature conditions possibly prevailing in the Martian core (Gudkova and Zharkov, 2004). If core size and density are specified, high core temperatures may cause iron to be enriched in the core because thermal expansion of

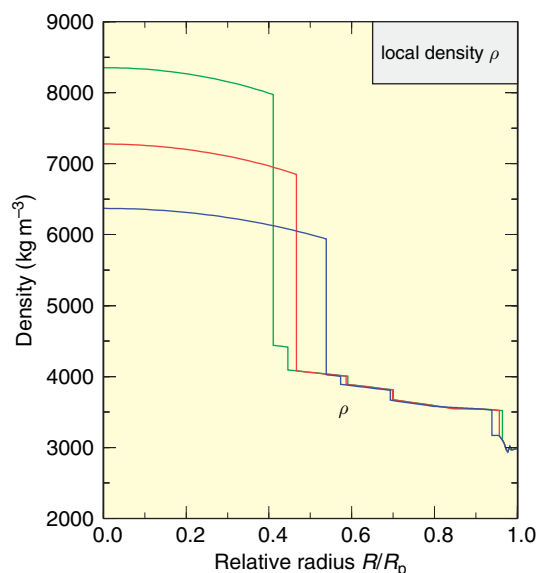


Figure 16 Radial density distribution of the Martian interior as a function of relative core radius R_c/R_p and core composition using the low-temperature crust model of Babeyko and Zharkov (2000). If the core were composed of pure iron (green), it would be small enough to enable the pressure-induced phase transformation from spinel to perovskite. In turn, a pure iron-sulfide core (blue) would be too large and mantle pressures, therefore, too low for the phase transition to occur. The intermediate density profile (red) refers to a Fe-FeS core containing iron and iron sulfide in equal amounts.

the main core constituents may exceed self-compression thereby increasing the planet's bulk Fe/Si ratio.

10.02.7.4 Mineralogy

Bertka and Fei (1997) obtained the sequence of mineralogical phase assemblages stable in the Martian mantle at elevated temperatures and up to core-mantle boundary pressures from high-pressure and high-temperature experiments using synthetic mineral mixtures according to the mantle composition of Dreibus and Wänke (1985). In Figure 17, it is seen that the upper part of the mantle then contains olivine, clinopyroxene, and garnet, whereas orthopyroxene is only present at pressures below 9 GPa. In the mantle transition zone at pressures above 13.5 GPa, β -spinel (wadsleyite) and clinopyroxene are subsequently replaced by γ -spinel (ringwoodite) and majorite until completion at about 17 GPa. A hot lower mantle is found to contain Mg-Fe silicate perovskite, magnesiowüstite, and majorite in the absence of CaSiO_3 perovskite (Bertka and Fei, 1997).

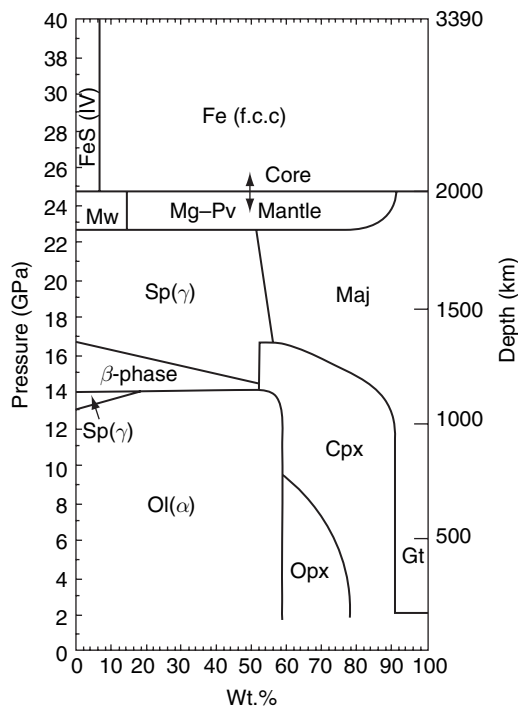


Figure 17 Mineral phase assemblages (in wt.%) of the Martian mantle as a function of pressure based on the chemical compositional model of [Dreibus and Wänke \(1985\)](#). Ol, olivine; Opx, orthopyroxene; Gt, garnet; Maj, majorite; Sp, spinel; Mw, magnesiowüstite; and Mg-Pv, Mg-Fe silicate perovskite. The location of the core-mantle boundary is from [Fei et al. \(1995\)](#). Adapted from Bertka CM and Fei Y (1997) Mineralogy of the Martian interior up to core-mantle boundary pressures. *Journal of Geophysical Research* 102: 5251–5264.

[Verhoeven et al. \(2005\)](#) have established empirical relationships between the most abundant mantle minerals based on a compilation of chemical compositions and related mineral assemblages of the silicate mantles of Mars and Earth. A perovskite layer at the base of the Martian mantle could only exist if pressures and temperatures in the mantle are sufficiently high for the occurrence of the mineral phase transitions. Therefore, the possible existence of a perovskite lower mantle and its stable phase assemblage in Mars not only depends on the core-mantle boundary pressure, that is, the size and composition of the core, but it is also sensitive to the temperature distribution deep inside the planet. [van Thienen et al. \(2006\)](#) have studied the stability range of such a putative perovskite lower mantle and its consequences for mantle plume dynamics, comparing the model mantle mineralogy from [Bertka and Fei \(1997\)](#) to

the model EH45 from [Sanloup et al. \(1999\)](#). Furthermore, uncertainties of a few 100 K in the experimental determinations of the pressure-temperature relation of the perovskite phase transformation and poor knowledge of the planet's thermal state ([Breuer and Spohn, 2003](#)) are taken into account. For a nominal core sulfur content of 14 wt.%, [van Thienen et al. \(2006\)](#) found that a perovskite layer sufficiently thick to affect mantle dynamics can be kept for both hot and cold mantle temperature profiles. Thus, it is feasible that at least in the early evolution of the planet, when mantle temperatures were much higher, a thin perovskite layer hovered above the core-mantle boundary. Additionally, data on the solid Fe-FeS system at high pressure and high temperature show a high-pressure, high-density phase change to a hexagonal NiAs superstructure at core pressures ([Fei et al., 1995](#)). This phase transition together with the assumed sulfur content in the Martian core of 12–16% of the core mass derived from the chemistry of the SNC meteorites also would imply a smaller core size and, in turn, an increase in thickness of a tentative perovskite lower mantle. Alternatively, a smaller size of the Martian core in favor of a deep perovskite layer is conceivable if a solid inner core composed of γ -iron would be present and surrounded by a less dense, volatile-rich liquid outer core.

If the geochemical requirement of a CI chondrite bulk composition is kept, the mantle density profile obtained from the experimentally determined sequence of mineralogical phase assemblages ([Bertka and Fei, 1997](#)) and a core density consistent with a core sulfur content of 14 wt.% would result in a mean moment of inertia factor of 0.354 ([Bertka and Fei, 1998a](#)). However, this model which lacks a perovskite layer at the base of the mantle requires a crust thickness of 180–320 km assuming a crustal density of 2700–3000 kg m⁻³. Since such a crust thickness is considered to be unrealistically large, a CI chondrite bulk composition of the Martian interior as assumed by [Dreibus and Wänke \(1985\)](#) may be questionable ([Bertka and Fei, 1998b](#)). Models using the same mantle density profile and a range of model core compositions but allowing for the moment of inertia factor of 0.3662 as obtained from the *Pathfinder* measurements generally produce bulk Fe/Si ratios below the CI chondrite value of 1.71. This may suggest that the formation of Mars and the terrestrial planets cannot be explained solely by the accretion

of CI carbonaceous chondrite material (Bertka and Fei, 1998b).

10.02.7.5 Martian Seismicity

A three-axis short-period seismometer onboard the Viking Lander 2 at Utopia Planitia collected more than 600 h of high-quality data to explore the seismic environment of Mars (Anderson *et al.*, 1976, 1977). The seismometer was added late in the mission planning, and therefore had to be installed on the top of the lander structure. Hence, wind noise contaminated the seismic data. No large seismic events were detected, indicating that Mars is less seismically active than Earth by an estimated three orders of magnitude. A seismic signal from one small quake was possibly recorded. Its tentative analysis suggested that it had a magnitude of 3 and had occurred at a distance of 110 km. Identification of late arrivals implied the presence of a crust with a thickness of 15 km near the landing site. However, it cannot be ruled out that wind gusts mimicked a seismic event.

While the seismicity of Mars is largely unexplored, there are indications that Mars could be quite active. Most morphological features on Mars seem to be only partially isostatically compensated

(Zuber *et al.*, 2000). These include the Tharsis rise as well as the Chryse and Amazonis basins. Regions of partial compensation on Earth are generally the most seismically active. Tectonic stresses implied by a lack of compensation are known to be in the 10- to 100-bar range and stress drops in earthquakes are in the same range. Hence, Mars could be tectonically active, though seismicity may be more localized. Based on a global compilation of compressional and extensional faults derived from MOLA shaded relief data, Knapmeyer *et al.* (2006) have constructed a new Martian seismicity model that predicts up to 25 seismic events per year with moment magnitudes greater than 4 corresponding to seismic moments $\geq 1.26 \times 10^{15}$ N m. Most of these events are expected to occur near the Tharsis rise but other seismic centers may be located south of Hellas and north of Utopia Planitia (Figure 18).

10.02.8 Venus

Venus, with a radius of 6051.8 km, is only slightly smaller than Earth, but the small size difference may have important consequences for the planet's interior.

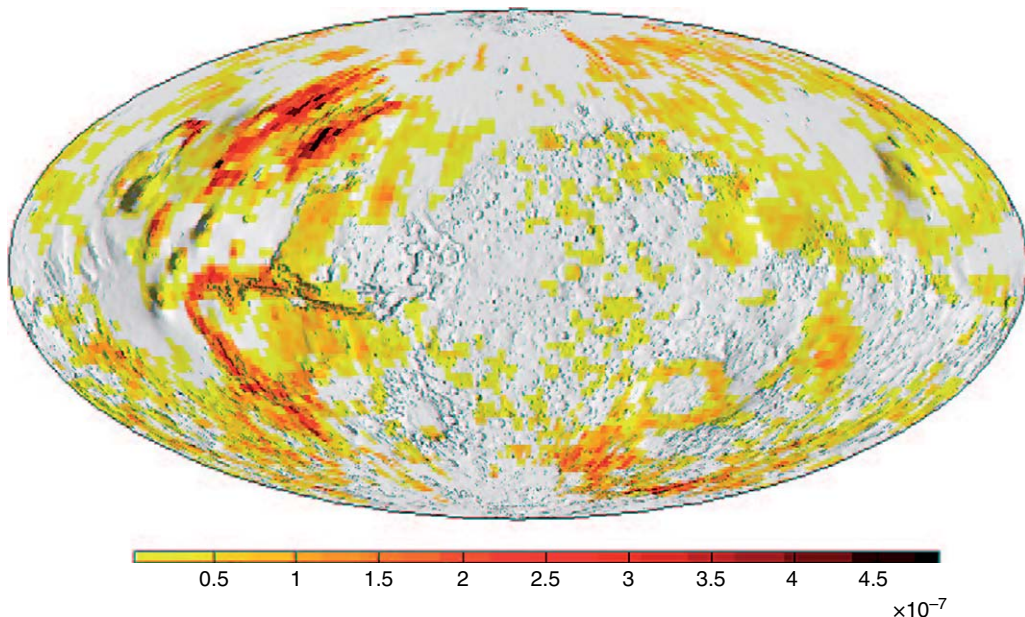


Figure 18 Global distribution of quake probability based on the distribution of extensional and compressional faults on Mars in units of faults per km^2 , irrespective of geologic age. Adapted from Knapmeyer M, Oberst J, Hauber E, Wählisch M, Deuchler C, and Wagner R (2006) Working models for spatial distribution and level of Mars' seismicity. *Journal of Geophysical Research* 111: E11006 (doi:10.1029/2006JE002708).

10.02.8.1 General

Unlike Earth, Venus has no magnetic field (Russell, 1980; Phillips and Russell, 1987; Donahue and Russell, 1997). This is likely a consequence of the smaller pressure at the center of Venus compared with the pressure at the center of Earth's core. Because of the lower pressure, it is possible that Venus' core has not yet cooled sufficiently to initiate inner-core growth, but has cooled enough to prevent the operation of a purely thermally driven dynamo (Stevenson *et al.*, 1983). Venus' lack of a magnetic field could also be due to its lack of plate tectonics, perhaps indicative of a sluggish form of mantle convection that is unable to cool the core efficiently enough to initiate thermal dynamo action (Nimmo and Stevenson, 2000). Still another possibility, though probably unlikely, is that the core of Venus has solidified enough that a dynamo cannot operate in the remaining liquid outer shell (Arkani-Hamed, 1994). Another consequence of Venus' slightly smaller size compared with Earth is that the perovskite–post-perovskite phase transition that occurs near the base of the Earth's mantle may not occur in Venus' mantle. If the core were to contain less light elements than the Earth's core, however, the Venusian mantle could be even deeper than that of the Earth.

10.02.8.2 Interior Structure

The above discussion tacitly assumed that the structure of Venus' interior is similar to that of the Earth, that is, that Venus is basically a three-layer body with a metallic core surrounded by a rocky mantle which is in turn surrounded by a compositionally distinct rocky crust. The basic structure of Venus is illustrated in Figure 19. However, the structure of the Venusian interior is a matter of some guesswork because we do not know the MoI of the planet and though spacecraft have visited Venus and landed on its surface, we have not yet seismically probed its interior. Because of the high pressure (≈ 95 bars) and temperature (≈ 737 K) at the surface of Venus (Seiff, 1983), a seismic experiment is probably far into the future. Venus' MoI is also something we will not know anytime soon. Venus lacks a moon to force a precession of the planet's retrograde spin axis, but the torque on the solar-induced tide forces a free precession ranging from 44.1 to $45.6'' \text{ yr}^{-1}$ and a variation of obliquity, or wobble, estimated at about $1.1'' \text{ yr}^{-1}$ (Yoder, 1997). Nevertheless, Venus is such a large terrestrial planet and would be heated so thoroughly

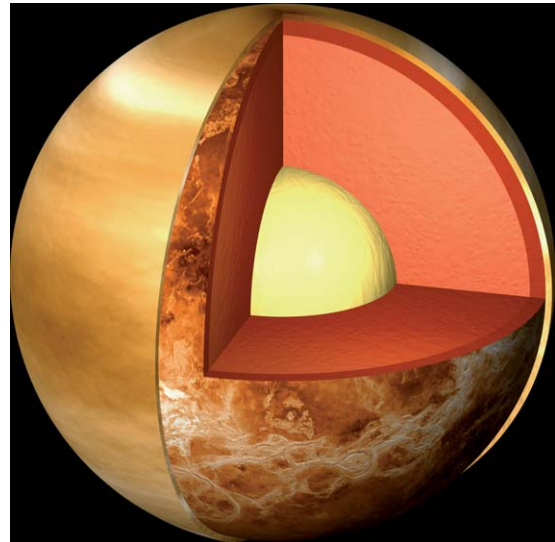


Figure 19 Cut-away view of the interior of Venus.
© Calvin J. Hamilton.

upon accretion, that differentiation into an Earth-like structure is all but inevitable. The extensive basaltic plains on Venus (Surkov, 1983; Weitz and Basilevsky, 1993; Basilevsky *et al.*, 1992; Campbell *et al.*, 1997) are evidence that it has differentiated a crust; it is even possible that plateau-like highlands such as Alpha Regio represent compositionally distinct pieces of crust.

Doppler radio tracking data of the Magellan and Pioneer Venus spacecraft have provided basic information about the planet's mass ($GM = 324858.6 \pm 0.014 \text{ km}^3 \text{ s}^{-2}$, G is the gravitational constant), gravitational field, and tidal Love number k_2 (Sjogren *et al.*, 1997). The Love number k_2 is determined from the time variations in the gravitational coefficients C_{22} and S_{22} at the solar period. Konopliv and Yoder (1996) have found $k_2 = 0.295 \pm 0.066$, a value consistent with a liquid core (Yoder, 1997). A 180 degree and order spherical harmonic model of Venus' gravity is given in Konopliv *et al.* (1999). Magellan radar altimetry data have been used to produce the 360 degree and order spherical harmonic model of Venus' topography presented in Rappaport *et al.* (1999) (see Chapter 10.5).

10.02.8.3 Composition

The predominantly basaltic nature of Venus' surface is suggested by the geochemical data obtained by the Venera and Vega landers and the morphology of the

widespread volcanic landforms (Grimm and Hess, 1997). The K/U and K/Th ratios of Venusian samples are similar to those obtained for terrestrial volcanics, SNC meteorites, and Martian samples. The variation of the K/U ratios at the seven landing sites is relatively narrow within a factor of three of each other implying that the volatile-refractory element inventory of Venus is comparable to that of Earth and Mars, but different from that of the Moon. The major oxide compositions of Venusian rocks are broadly consistent with those of basaltic rocks so that it is reasonable to assume that the crust is largely basaltic (Grimm and Hess, 1997). The gravity and topography data can be analyzed to provide information on the average thickness of the crust; estimates lie in the range 20–50 km (Grimm and Hess, 1997; Nimmo and McKenzie, 1998). The crust is thicker (45–85 km) beneath the plateau highlands (Alpha, Ovda, Thetis, and Tellus Regiones) (Moore and Schubert, 1997) compared with other regions. The basalt–eclogite phase change limits the crustal thickness to about 50 km for moderate conductive geotherms of $>5\text{--}10\text{ K km}^{-1}$ (Grimm and Hess, 1997). The Venusian gravity and topography data have also been used to infer values for the thickness of the planet's thermal lithosphere and its elastic upper layer. Estimates of lithosphere thickness vary between about 200 and 400 km with thinner lithosphere beneath volcanic highlands (e.g., Atla and Beta Regiones) (Moore and Schubert, 1997; Kucinkas and Turcotte, 1994; Phillips, 1994; Smrekar, 1994; Simons *et al.*, 1994; Herrick *et al.*, 1989). Lithospheric thinning beneath the volcanic rises could have been caused by mantle plumes. There is buoyant sublithospheric mantle beneath the volcanic rises (Moore and Schubert, 1997). The top part of the lithosphere that behaves elastically is only about 30 km thick (McKenzie and Nimmo, 1997). Unlike on Earth, gravity anomalies correlate with high topography on Venus.

10.02.8.4 Tectonism

Pioneer Venus radar, Earth-based radar observations, Venera 15–16 orbital imaging radar, and Magellan radar images have provided views of the surface of Venus unimpeded by the global cloud cover that prevents visual observation. These views, together with the topography and gravity data, reveal the nature of Venusian tectonism and volcanism. On Earth, the global oceanic rift system and the arcuate ocean trenches are the primary surface

manifestations of plate tectonics. The almost total absence of these features on Venus has led to the conclusion that active plate tectonics is not occurring on Venus (Kaula and Phillips, 1981; Kaula, 1994). At the present time Venus is a one-plate planet. Nevertheless, there are tectonic features on Venus that resemble major tectonic features on Earth. Beta Regio, a volcanic highland, has many of the features of a continental rift on Earth. It has a domal structure with a diameter of about 2000 km and a swell amplitude of about 2 km. It has a well-defined central rift valley with a depth of 1–2 km and there is some evidence for a three-armed planform (aulacogen). Alta, Eistla, and Bell Regiones have similar rift zone characteristics (Grimm and Phillips, 1992; Senske *et al.*, 1992). Aphrodite Terra with a length of some 1500 km is reminiscent of major continental collision zones on Earth, such as the mountain belt that extends from the Alps to the Himalayas. Ishtar Terra is a region of elevated topography with a horizontal scale of 2000–3000 km. A major feature is Lakshmi Planum, which is an elevated plateau similar to Tibet with a mean elevation of about 4 km. This plateau is surrounded by linear mountain belts, Akna, Danu, Freyja, and Maxwell montes, reaching elevations of 10 km, similar in scale and elevation to the Himalayas (Kaula *et al.*, 1997).

10.02.8.5 Dynamics

The impact crater population on the surface of Venus has been used to infer a mean surface age of several hundred to as much as 800 Myr (McKinnon *et al.*, 1997; Herrick *et al.*, 1997). It has been proposed that the relatively young age of Venus' surface was set in a global volcanic resurfacing event and that relatively little volcanism has occurred since (Schaber *et al.*, 1992; Basilevsky *et al.*, 1997). The resurfacing event could be the means by which Venus expels its heat. One way this could happen is the global foundering of a thick, relatively cold and heavy lithosphere and its replacement by the relatively hot underlying mantle (Turcotte, 1993). Such events might have occurred episodically throughout Venus' history. Between such events the lithosphere would thicken but Venus would have no efficient way, like plate tectonics on Earth, to expel its heat. Instead the heat building up in the interior during the quiescent period would be lost in the mantle overturn when the lithosphere thickened enough to become gravitationally unstable. The initiation of such an event might be evident today on Venus' surface in the form of

large coronae. Coronae are quasi-circular features, 100–2600 km in diameter, with raised interiors and elevated rims, often with annular troughs (Stofan *et al.*, 1997). McKenzie *et al.* (1992) and Sandwell and Schubert (1992a, 1992b) have argued that the perimeters of several large coronae on Venus, specifically Artemis, Latona, and Eithinoa, resemble terrestrial subduction zones in both planform and topography. Artemis chasma has a radius of curvature similar to that of the South Sandwich subduction zone on the Earth. Sandwell and Schubert (1992a) proposed that the large coronae are incipient circular subduction zones. The foundering lithosphere is replaced by ascending hot mantle in a manner similar to back-arc spreading on the Earth. A single global resurfacing event for Venus has been challenged by Hauck *et al.* (1998). They argue that the interpretation of the Venusian crater distribution is nonunique and they identify some units in the volcanic plains that have a spread in age of about 0.5 Gyr.

Because Venus lacks plate tectonics, convection in its mantle is different from the style of convection in Earth's mantle. Venusian mantle convection occurs in the sluggish or stagnant lid regime, that is, it is confined below the lithosphere or nearly rigid lid (Schubert *et al.*, 1997). This form of convection is less efficient at transporting heat than is the plate tectonic regime with consequent implications for the thermal history of the planet and the dynamics of its core, as noted above. Mantle convection in Venus may be unable to establish a near equilibrium with its internal heat sources resulting in the episodic overturning of its mantle and global resurfacing. Enhanced core cooling would occur during such an event with the possible initiation of a transient dynamo. Heat from the core would be carried away by mantle plumes that could form volcanic rises similar to Atla and Beta Regionis.

10.02.9 Summary and Outlook

The terrestrial planets Mercury, Venus, Earth, and Mars have low masses, small radii, and large densities in comparison to the giant planets in the outer solar system. This is also true for terrestrial-type bodies like the Moon and some of the outer planet satellites and it provides important clues on their bulk compositions. Rotational, gravitational, and magnetic field observations indicate that the interiors of these bodies are strongly differentiated and subdivided like that of the Earth into iron-rich cores, silicate

mantles, and rocky crusts derived from partial mantle melts. Isotope data reveal that the cores and the primary crusts formed early and rapidly. Geodetic observations of the rotational state and/or tidal response suggest that the interiors are warm enough to maintain liquid outer core shells or entirely liquid cores. For Mars, Venus, and Earth, mantle pressures are sufficient to permit mineral phase transformations from olivine and pyroxene assemblages to spinel or even perovskite and post-perovskite phases. Since the phase transition depths also depend on the ambient temperature and the iron content of the mantle rocks, future seismological observations have the potential to provide additional information on the thermal states and compositional differences of the terrestrial planets. Single-plate planets, the Moon, Mercury, Mars, and Venus, are believed to be cooling by lithospheric thickening while the deep interior remains relatively warm. It is likely, therefore, that due to the progressive cooling of the planet's outer portion, thermoelastic stresses will be occasionally released at preexisting faults thereby causing local seismic activity at a level detectable by seismometers.

Future developments will benefit from the combination of classic forward modeling techniques and Bayesian probabilistic inversion methods as more spacecraft and laboratory data are being collected that considerably extend the database required to construct planetary interior models. The inverse problem is commonly based on nonlinear relations between model and data. Uncertainties of observed and calculated parameters have to be taken into account, as well as *a priori* knowledge such as the possible range of surface composition as obtained from remote-sensing observations and *in situ* measurements. This has been detailed by Khan *et al.* (2007) who have directly inverted geophysical observations – including the lunar mass and MoI, the Apollo seismic data set, and long-period electromagnetic sounding data – for the chemical composition, mantle mineralogy, and thermal state of the Moon. A Markov chain Monte Carlo algorithm is applied to perform the joint inversion of these data sets. The calculation of mineral phase equilibria in the CFMAS system comprising rock-forming oxides $\text{CaO-FeO-MgO-Al}_2\text{O}_3\text{-SiO}_2$ is based on Gibbs energy minimization schemes (Kuskov and Galimzyanov, 1986).

Future space telescope missions like *Kepler* and *COROT* are expected to detect many super-massive terrestrial-type exoplanets in the coming years. From

combined photometric transit observations and Doppler radial velocity measurements, mass and radius of a transiting exoplanet will be obtained and reliable estimates of its mean density derived (see Chapter 10.13). It is necessary, therefore, to establish mass–radius relations of massive terrestrial-type bodies for comparison with these new observational data. The mass–radius relation of these objects is likely to deviate from a cubic power law for constant-density scaling due to large self-compression and higher internal temperatures. Valencia *et al.* (2006) have developed scaling laws for the interiors of super-massive terrestrial exoplanets yielding their total radius, mantle thickness, core size, and mean density as a function of total mass. For Super-Earths, a relation between total radius R and mass M like $R \propto M^{0.267-0.272}$ has been suggested. Furthermore, it is seen that uncertainties that are linked to thermodynamic EOS parameters do not significantly alter the scaling exponents of bulk properties at a given pressure regime. In contrast, the scaling exponents are mainly affected by compositional differences (super-massive rock, metal, ice/water bodies). This implies that the bulk compositions of transiting super-massive terrestrial-type exoplanets could be measured soon by using Earth-orbiting space telescopes (Valencia *et al.*, 2007).

Acknowledgments

The authors thank Tamara Gudkova, Martin Knapmeyer, and Jürgen Oberst for helpful discussions and acknowledge constructive criticisms from Tim Van Hoolst, Mark Wieczorek, and Tilman Spohn. Some figures in this chapter were produced by using the Generic Mapping Tools (GMT) of Wessel and Smith (1991).

References

- Acuña MH, Connerney JEP, Wasilewski P, *et al.* (1998) Magnetic field and plasma observations at Mars: Initial results of the Mars global surveyor mission. *Science* 279: 1676–1680.
- Acuña MH, Connerney JEP, Ness NF, *et al.* (1999) Global distribution of crustal magnetization discovered by the Mars global surveyor MAG/ER experiment. *Science* 284: 790–793.
- Anderson DL (1989) *Theory of the Earth*. Cambridge, MA: Blackwell.
- Anderson DL, Miller WF, Latham GV, *et al.* (1976) The Viking seismic experiment. *Science* 194: 1317–1321.
- Anderson DL, Miller WF, Latham GV, *et al.* (1977) Seismology on Mars. *Journal of Geophysical Research* 82: 4524–4546.
- Anderson JD, Colombo G, Esposito PB, Lau EL, and Trager GB (1987) The mass, gravity field, and ephemeris of Mercury. *Icarus* 71: 337–349.
- Anderson JD, Jurgens RF, Lau EL, Slade MA, III, and Schubert G (1996) Shape and orientation of Mercury from radar ranging data. *Icarus* 124: 690–697.
- Anderson JD and Schubert G (2007) Saturn's satellite Rhea is a homogeneous mix of rock and ice. *Geophysical Research Letters* 34: L02202.
- Anderson OL (1984) A universal thermal equation-of-state. *Journal of Geodynamics* 1: 185–214.
- Anderson OL, Isaak DG, and Oda H (1992) High-temperature elastic constant data on minerals relevant to geophysics. *Reviews of Geophysics* 30: 57–90.
- Arkani-Hamed J (1994) On the thermal evolution of Venus. *Journal of Geophysical Research* 99: 2019–2033.
- Babeyko AY and Zharkov VN (2000) Martian crust: A modeling approach. *Physics of the Earth and Planetary Interiors* 117: 421–435.
- Badding JV, Hemley RJ, and Mao HK (1991) High-pressure chemistry of hydrogen in metals: *In situ* study of iron hydride. *Science* 253: 421–424.
- Balog PS, Secco RA, Rubie DC, and Frost DJ (2003) Equation of state of liquid Fe–10 wt% S: Implications for the metallic cores of planetary bodies. *Journal of Geophysical Research* 108(B2): 2124 (doi:10.1029/2001JB001646).
- Balogh A and Giampieri G (2002) Mercury: The planet and its orbit. *Reports of Progress in Physics* 65: 529–560.
- Banks R (1969) Geomagnetic variations and the electrical conductivity of the upper mantle. *Geophysical Journal of the Royal Astronomical Society* 17: 457–487.
- Basilevsky AT, Nikolaeva OV, and Weitz CM (1992) Geology of the Venera-8 landing site region from Magellan data – Morphological and geochemical considerations. *Journal of Geophysical Research* 97(E10): 16,315–16,335.
- Basilevsky AT, Head JW, Schaber GG, and Strom RG (1997) The resurfacing history of Venus. In: Bougher SW, Hunten DM, and Phillips RJ (eds.) *Venus II: Geology, Geophysics, Atmosphere, and Solar Wind Environment*, pp. 1047–1084. Tucson, AZ: University of Arizona Press.
- Bass J (2004) *Current and Future Research Directions in High-Pressure Mineral Physics*. Consortium for Materials Properties Research in Earth Sciences (COMPRES), Stony Brook, NY.
- Belleguic V, Lognonné P, and Wieczorek M (2005) Constraints on the Martian lithosphere from gravity and topography data. *Journal of Geophysical Research* 110: E11005 (doi:10.1029/2005JE002437).
- Bertka CM and Fei Y (1997) Mineralogy of the Martian interior up to core–mantle boundary pressures. *Journal of Geophysical Research* 102: 5251–5264.
- Bertka CM and Fei Y (1998a) Density profile of an SNC model Martian interior and the moment of inertia factor of Mars. *Earth and Planetary Science Letters* 157: 79–88.
- Bertka CM and Fei Y (1998b) Implications of Mars Pathfinder data for the accretion history of the terrestrial planets. *Science* 281: 1838–1840.
- Bills BG and Ferrari AJ (1977) A lunar density model consistent with topographic, gravitational, librational, and seismic data. *Journal of Geophysical Research* 82: 1306–1314.
- Bills BG, Neumann GA, Smith DE, and Zuber MT (2005) Improved estimate of tidal dissipation within Mars from MOLA observations of the shadow of Phobos. *Journal of Geophysical Research* 110: E07004 (doi:10.1029/2004JE002376).
- Bina CR and Helffrich GR (1992) Calculation of elastic properties from thermodynamic equation of state principles. *Annual Review of Earth and Planetary Sciences* 20: 527–552.

- Binder AB (1998) Lunar prospector: Overview. *Science* 281: 1475–1476.
- Blewett DT, Lucey PG, Hawke BR, Ling GG, and Robinson MS (1997) A comparison of Mercurian reflectance and spectral quantities with those of the Moon. *Icarus* 129: 217–231.
- Boehler R (1992) Melting of the Fe–FeO and the Fe–FeS systems at high pressure: Constraints on core temperatures. *Earth and Planetary Science Letters* 111: 217–227.
- Boehler R (1996a) Fe–FeS eutectic temperatures to 620 kbar. *Physics of the Earth and Planetary Interiors* 96: 181–186.
- Boehler R (1996b) Melting of mantle and core materials at very high pressures. *Philosophical Transactions of the Royal Society of London A* 354: 1265–1278.
- Boehler R (1996c) Melting temperature of the Earth's mantle and core: Earth's thermal structure. *Annual Review of Earth and Planetary Sciences* 24: 15–40.
- Breuer D and Spohn T (2003) Early plate tectonics versus single-plate tectonics on Mars: Evidence for magnetic field history and crust evolution. *Journal of Geophysical Research* 108(E7): 5072 (doi:10.1029/2002JE001999).
- Britt DT and Consolmagno GJ (2003) Stony meteorite porosities and densities: A review of the data through 2001. *Meteorites and Planetary Science* 38: 1161–1180.
- Brückner J, Dreibus G, Rieder G, and Wänke H (2003) Refined data of Alpha-Proton-X-ray spectrometer analyses of soils and rocks at the Mars Pathfinder site: Implications for surface chemistry. *Journal of Geophysical Research* 108(E12): 8094 (doi:10.1029/2003JE002060).
- Burns JA (1976) Consequences of the tidal slowing of Mercury. *Icarus* 28: 453–458.
- Bussey DBJ and Spudis PD (2000) Compositional studies of the Orientale, Humorum, Nectaris, and Crisium lunar basins. *Journal of Geophysical Research* 105: 4235–4244.
- Cameron AGW, Fegley B, Benz W, and Slattery WL (1988) The strange density of Mercury: Theoretical considerations. In: Vilas F, Chapman CR, and Matthews MS (eds.) *Mercury*, pp. 692–708. Tucson, AZ: University of Arizona Press.
- Campbell BA, Arvidson RE, Shepard MK, and Brackett RA (1997) Remote sensing of surface processes. In: Bougher SW, Hunten DM, and Philips RJ (eds.) *Venus II: Geology, Geophysics, Atmosphere, and Solar Wind Environment*, pp. 503–526. Tucson, AZ: University of Arizona Press.
- Chapman S and Price AT (1930) The electric and magnetic state of the interior of the earth, as inferred from terrestrial magnetic variations. *Philosophical Transactions of the Royal Society of London Series A* 229: 0427–0460.
- Chase SC, Miner ED, Morrison D, Münch G, and Neugebauer G (1976) Mariner 10 infrared radiometer results: Temperatures and thermal properties of the surface of Mercury. *Icarus* 28: 565–578.
- Chenet H, Lognonné P, Wieczorek M, and Mizutani H (2006) Lateral variations of lunar crustal thickness from the Apollo seismic data set. *Earth and Planetary Science Letters* 243: 1–14.
- Connerney JEP, Acuña MH, Ness NF, Spohn T, and Schubert G (2004) Mars crustal magnetism. *Space Science Review* 111: 1–32.
- Connerney JEP, Acuña MH, Ness NF, *et al.* (2005) Tectonic implications of Mars crustal magnetism. *Proceedings of the National Academy of Sciences of the United States of America* 102: 14,970–14,975.
- Connerney JEP, Acuña MH, Wasilewski PJ, *et al.* (1999) Magnetic lineations in the ancient crust of Mars. *Science* 284: 794–798.
- Connerney JEP, Acuña MH, Wasilewski PJ, *et al.* (2001) The global magnetic field of Mars and implications for crustal evolution. *Geophysical Research Letters* 28: 4015–4018.
- Constable S and Constable C (2004) Observing geomagnetic induction in magnetic satellite measurements and associated implications for mantle conductivity. *Geochemistry, Geophysics, Geosystems* 5: Q01006.
- Conzelmann V (1994) *Thermische Evolution des Planeten Merkur berechnet unter Anwendung verschiedener Viskositätsgesetze*. PhD Thesis, Institut für Planetologie, Westfälische Wilhelms-Universität, Münster.
- Dehant V, Defraigne P, and Hoolst TV (2000) Computation of Mars' transfer function for nutations, tides, and surface loading. *Physics of the Earth and Planetary Interiors* 117: 385–395.
- Dickey JO, Bender PL, Faller JE, *et al.* (1994) Lunar laser ranging: A continuing legacy of the Apollo program. *Science* 265: 482–490.
- Donahue TM and Russell CT (1997) The Venus atmosphere and ionosphere and their interaction with the solar wind: An overview. In: Bougher SW, Hunten DM, and Philips RJ (eds.) *Venus II: Geology, Geophysics, Atmosphere, and Solar Wind Environment*, pp. 3–31. Tucson, AZ: University of Arizona Press.
- Drake MJ (2001) The eucrite/Vesta story. *Meteoritics* 36: 501–513.
- Dreibus G and Wänke H (1985) Mars: A volatile rich planet. *Meteoritics* 20: 367–382.
- Elkins-Tanton LT, Chatterjee N, and Grove TL (2003a) Experimental and petrologic constraints on lunar differentiation from the Apollo 15 green picritic glasses. *Meteorites and Planetary Science* 38: 515–527.
- Elkins-Tanton LT, Parmentier EM, and Hess PC (2003b) Magma ocean fractional crystallization and cumulate overturn in terrestrial planets: Implications for Mars. *Meteorites and Planetary Science* 38: 1753–1771.
- Elphic RC and Russell CT (1978) On the apparent source depth of planetary magnetic fields. *Geophysical Research Letters* 5: 211–214.
- Esposito PB, Banerdt WB, Lindal GF, *et al.* (1992) Gravity and topography. In: Kieffer HH, Jakosky BM, Snyder CW, and Matthews MS (eds.) *Mars*, pp. 209–248. Tucson, AZ: University of Arizona Press.
- Fei Y, Prewitt CT, Mao HK, and Bertka CM (1995) Structure and density of FeS at high pressure and high temperature and the internal structure of Mars. *Science* 268: 1892–1894.
- Fei Y, Bertka CM, and Finger LW (1997) High-pressure iron-sulfur compound, Fe₃S₂, and melting relations in the Fe–FeS system. *Science* 268: 1621–1623.
- Folkner WM, Yoder CF, Yuan DN, Standish EM, and Preston RA (1997) Interior structure and seasonal mass redistribution of Mars from radio tracking of Mars Pathfinder. *Science* 278: 1749–1752.
- Frey HV, Roark JH, Shockey KM, Frey EL, and Sakimoto SEH (2002) Ancient lowlands on Mars. *Geophysical Research Letters* 29(10): 1384 (doi:10.1029/2001GL013832).
- Ghosh A and McSween HJ, Jr. (1998) A thermal model for the differentiation of asteroid 4 Vesta, based on radiogenic heating. *Icarus* 134: 187–206.
- Goettel KA (1988) Present bounds on the bulk composition of Mercury: Implications for planetary formation processes. In: Vilas F, Chapman CR, and Matthews MS (eds.) *Mercury*, pp. 613–621. Tucson, AZ: University of Arizona Press.
- Goins NR, Dainty AM, and Toksöz MN (1981) Lunar seismology: The internal structure of the Moon. *Journal of Geophysical Research* 86: 5061–5074.
- Grasset O, Sotin C, and Deschamps F (2000) On the internal structure and dynamics of Titan. *Planetary and Space Sciences* 48: 617–636.
- Grimm RE and Hess PC (1997) The crust of Venus. In: Bougher SW, Hunten DM, and Philips RJ (eds.) *Venus II: Geology, Geophysics, Atmosphere, and Solar Wind*

- Environment*, pp. 1205–1244. Tucson, AZ: University of Arizona Press.
- Grimm RE and Phillips RJ (1992) Anatomy of a Venusian hot-spot – Geology, gravity, and mantle dynamics of Eistla Regio. *Journal of Geophysical Research* 97(E10): 378–388.
- Gudkova TV and Zharkov VN (2004) Mars: Interior structure and excitation of free oscillations. *Physics of the Earth and Planetary Interiors* 142: 1–22.
- Hale AS and Hapke B (2002) A time-dependent model of radiative and conductive thermal energy transport in planetary regoliths with applications to the Moon and Mercury. *Icarus* 156: 318–334.
- Halekas JS, Mitchell DL, Lin RP, *et al.* (2001) Mapping of crustal magnetic anomalies on the lunar near side by the Lunar Prospector electron reflectometer. *Journal of Geophysical Research* 106(E11): 27841–27852.
- Harder H and Schubert G (2001) Sulfur in Mercury's core? *Icarus* 151: 118–122.
- Harmon JK, Perillat PJ, and Slade MA (2001) High-resolution radar imaging of Mercury's north pole. *Icarus* 149: 1–15.
- Hauck SA, Dombard AJ, Phillips RJ, and Solomon SC (2004) Internal and tectonic evolution of Mercury. *Earth and Planetary Science Letters* 222: 713–728.
- Hauck SA, Phillips RJ, and Price MH (1998) Venus: Crater distribution and plains resurfacing models. *Journal of Geophysical Research* 103(E6): 13635–13642.
- Head JW, Kreslavsky MA, and Pratt S (2002) Northern lowlands of Mars: Evidence for widespread volcanic flooding and tectonic deformation in the Hesperian Period. *Journal of Geophysical Research* 107(E1): 5003 (doi:10.1029/2001JE001445).
- Heiken G, Vaniman D, and French BM (1991) *The Lunar Sourcebook*. New York: Cambridge University Press.
- Hemley RJ (2006) Erskine Williamson, extreme conditions, and the birth of mineral physics. *Physics Today* 59: 50–56.
- Hemley RJ and Ashcroft NW (1998) The revealing role of pressure in the condensed matter sciences. *Physics Today* 51: 26–32.
- Herrick RR, Bills BG, and Hall SA (1989) Variations in effective compensation depth across Aphrodite Terra, Venus. *Geophysical Research Letters* 16: 543–546.
- Herrick RR, Sharpton VL, Malin MC, Lyons SN, and Feely K (1997) Morphology and morphometry of impact craters. In: Bougher SW, Hunten DM, and Phillips RJ (eds.) *Venus II: Geology, Geophysics, Atmosphere, and Solar Wind Environment*, pp. 1015–1046. Tucson, AZ: University of Arizona Press.
- Hiesinger H, Head JW, Wolf U, Jaumann R, and Neukum G (2003) Ages and stratigraphy of mare basalts in Oceanus Procellarum, Mare Nubium, Mare Cognitum, and Mare Insularum. *Journal of Geophysical Research* 108(E7): 5065 (doi:10.1029/2002JE001985).
- Hobbs BA (1987) Conductivity profiles from global data. *Pure and Applied Geophysics* 125: 393–407.
- Hofmeister AM (1991) Pressure derivatives of the bulk modulus. *Journal of Geophysical Research* 96: 21893–21907.
- Hood LL (1986) Geophysical constraints on the lunar interior. In: Phillips RJ, Hartmann WK, and Taylor GJ (eds.) *Origin of the Moon*, pp. 397–409. Houston: Lunar and Planetary Institute.
- Hood LL, Herbert F, and Sonett CP (1982) The deep lunar electrical conductivity profile – Structural and thermal inferences. *Journal of Geophysical Research* 87: 5311–5326.
- Hood LL and Huang Z (1991) Formation of magnetic anomalies antipodal to lunar impact basins: Two-dimensional model calculations. *Journal of Geophysical Research* 96: 9837–9846.
- Hood LL and Jones JH (1987) Geophysical constraints on lunar bulk composition and structure: A reassessment. *Proceedings of the 17th Lunar and Planetary Science Conference Part 2, Journal of Geophysical Research* 92: E396–E410.
- Hood LL, Mitchell DL, Lin RP, Acuna MH, and Binder AB (1999) Initial measurements of the lunar induced magnetic dipole moment using Lunar Prospector magnetometer data. *Geophysical Research Letters* 26: 2327–2330.
- Hood LL and Sonett CP (1982) Limits on the lunar temperature profile. *Geophysical Research Letters* 9: 37–40.
- Hood LL, Zakharian A, Halekas J, *et al.* (2001) Initial mapping and interpretation of lunar crustal magnetic anomalies using Lunar Prospector magnetometer data. *Journal of Geophysical Research* 106(E11): 27825–27839.
- Hood LL and Zuber MT (2000) Recent refinements in geophysical constraints on lunar origin and evolution. In: Canup RM and Righter K (eds.) *Origin of the Earth and Moon*, pp. 397–409. Tucson, AZ: University of Arizona Press.
- Husmann H, Sohl F, and Spohn T (2006) Subsurface oceans and deep interiors of medium-sized outer planet satellites and large trans-neptunian objects. *Icarus* 185: 258–273.
- Jarvis GT and Peltier WR (1989) Convection models and geophysical observations. In: Peltier WR (ed.) *Mantle Convection: Plate Tectonics and Global Dynamics*, pp. 479–593. New York: Gordon and Breach.
- Jeanloz R, Mitchell DL, Sprague AL, and de Pater I (1995) Evidence for a basalt-free surface on Mercury and implications for internal heat. *Science* 268: 1455–1457.
- Jehn R, Corral C, and Giampieri G (2004) Estimating Mercury's 88-day libration amplitude from orbit. *Planetary and Space Sciences* 52: 727–732.
- Jolliff BL, Gillis JJ, Haskin LA, Korotev RL, and Wieczorek MA (2000a) Major lunar crustal terranes: Surface expressions and crust-mantle origins. *Journal of Geophysical Research* 105: 4197–4216.
- Jolliff BL, Gaddis LR, Ryder G, *et al.* (2000b) New views of the Moon: Improved understanding through data integration. *EOS Transactions of the American Geophysical Union* 81(349): 354–355.
- Kaula WM (1979) The moment of inertia of Mars. *Geophysical Research Letters* 6: 194–196.
- Kaula WM (1994) The tectonics of Venus. *Philosophical Transactions of the Royal Society of London, Series A* 349: 345–355.
- Kaula WM, Drake MJ, and Head JW (1986) The Moon. In: Burns JA and Matthews MS (eds.) *Satellites*, pp. 581–628. Tucson, AZ: University of Arizona Press.
- Kaula WM, Lenardic A, Bindshchadler DL, and Arkani-Hamed J (1997) Ishtar terra. In: Bougher SW, Hunten DM, and Phillips RJ (eds.) *Venus II: Geology, Geophysics, Atmosphere, and Solar Wind Environment*, pp. 879–900. Tucson, AZ: University of Arizona Press.
- Kaula WM and Phillips RJ (1981) Quantitative tests for plate tectonics on Venus. *Geophysical Research Letters* 8: 1187–1190.
- Kaula WM, Schubert G, Lingenfelter RE, Sjogren WL, and Wollenhaupt WR (1974) Apollo laser altimetry and inferences as to the lunar structure. *Proceedings of the 5th Lunar and Planetary Science Conference*, Vol. 3, pp. 3049–3058. Pergamon Press.
- Kavner A, Duffy TS, and Shen G (2001) Phase stability and density of FeS at high pressures and temperatures: Implications for the interior structure of Mars. *Earth and Planetary Science Letters* 185: 25–33.
- Keil K (2002) Geological history of asteroid 4 Vesta. In: Bottke WF, Paolicchi P, Binzel RP, and Cellino A (eds.) *Asteroids III*, pp. 573–584. Tucson, AZ: University of Arizona Press.
- Khan A and Mosegaard K (2002) An inquiry into the lunar interior: A nonlinear inversion of the Apollo lunar seismic

- data. *Journal of Geophysical Research* 107(E6): 50036 (doi:10.1029/2001JE001658).
- Khan A, Mosegaard K, and Rasmussen KL (2000) A new seismic velocity model for the Moon from a Monte Carlo inversion of the Apollo lunar seismic data. *Geophysical Research Letters* 27: 1591–1594.
- Khan A, Mosegaard K, Williams JG, and Lognonné P (2004) Does the moon possess a molten core? Probing the deep lunar interior using results from LLR and Lunar Prospector. *Journal of Geophysical Research* 109(E09): E09007 (doi:10.1029/2004JE002294).
- Khan A, MacLennan J, Taylor SR, and Connolly JAD (2006a) Are the Earth and the moon compositionally alike? Inferences on lunar composition and implications for lunar origin and evolution from geophysical modeling. *Journal of Geophysical Research* 111(E05): E05005 (doi:10.1029/2005JE002608).
- Khan A, Connolly JAD, Olsen N, and Mosegaard K (2006b) Constraining the composition and thermal state of the moon from an inversion of electromagnetic lunar day-side transfer functions. *Earth and Planetary Science Letters* 248: 579–598.
- Khan A, Connolly JAD, MacLennan J, and Mosegaard K (2007) Joint inversion of seismic and gravity data for lunar composition and thermal state. *Geophysical Journal International* 168: 243–258.
- Khurana KK, Kivelson MG, Stevenson DJ, et al. (1998) Induced magnetic fields as evidence for subsurface oceans in Europa and Callisto. *Nature* 395: 777–780.
- Kivelson MG, Bagenal F, Kurth WS, Neubauer FM, Paranicas C, and Saur J (2004) Magnetospheric interactions with satellites. In: Bagenal F, Dowling T, and McKinnon W (eds.) *Jupiter, The Planet, Satellites, and Magnetosphere*, pp. 513–536. Cambridge UK: Cambridge University Press.
- Kivelson MG, Khurana KK, Stevenson DJ, et al. (1999) Europa and Callisto: Induced or intrinsic fields in a periodically varying plasma environment. *Journal of Geophysical Research* 104(A3): 4609–4626.
- Kivelson MG, Khurana KK, Russell CT, Volwerk M, Walker RJ, and Zimmer C (2000) Galileo magnetometer measurements: A stronger case for a subsurface ocean at Europa. *Science* 289: 1340–1343.
- Kivelson MG, Khurana KK, and Volwerk M (2002) The permanent and inductive magnetic moments of Ganymede. *Icarus* 157: 507–522.
- Kleine T, Münker C, Mezger K, and Palme H (2002) Rapid accretion and early core formation on asteroids and the terrestrial planets from Hf-W chronometry. *Nature* 418: 952–955.
- Knapmeyer M, Oberst J, Hauber E, Wählisch M, Deuchler C, and Wagner R (2006) Working models for spatial distribution and level of Mars's seismicity. *Journal of Geophysical Research* 111: E11006 (doi:10.1029/2006JE002708).
- Konopliv AS, Asmar SW, Carranza E, Sjogren WL, and Yuan DN (2001) Recent gravity models as a result of the Lunar Prospector mission. *Icarus* 150: 1–18.
- Konopliv AS, Banerdt WB, and Sjogren WL (1999) Venus gravity: 180th degree and order model. *Icarus* 139: 3–18.
- Konopliv AS, Binder AB, Hood LL, Kucinskas AB, Sjogren WL, and Williams JG (1998) Improved gravity field of the Moon from Lunar Prospector. *Science* 281: 1476–1480.
- Konopliv AS and Yoder CF (1996) Venusian k_2 tidal Love number from Magellan and PVO tracking data. *Geophysical Research Letters* 23: 1857–1860.
- Konopliv AS, Yoder CF, Standish EM, Yuan DN, and Sjogren WL (2006) A global solution for the Mars static and seasonal gravity, Mars orientation, Phobos and Deimos masses, and Mars ephemeris. *Icarus* 182: 23–50.
- Korotev RL (2005) Lunar geochemistry as told by lunar meteorites. *Chemie der Erde-Geochemistry* 65: 297–346.
- Kovach RL and Chyba CF (2001) Seismic detectability of a subsurface ocean on Europa. *Icarus* 150: 279–287.
- Kucinskas AB and Turcotte DL (1994) Isostatic compensation of equatorial highlands on Venus. *Icarus* 112: 104–116.
- Kuskov OL (1995) Constitution of the Moon: 3. Composition of the middle mantle from seismic data. *Physics of the Earth and Planetary Interiors* 90: 55–74.
- Kuskov OL (1997) Constitution of the Moon: 4. Composition from the mantle from seismic data. *Physics of the Earth and Planetary Interiors* 102: 239–257.
- Kuskov OL and Fabrichnaya OB (1995) Constitution of the Moon: 2. Composition and seismic properties of the lower mantle. *Physics of the Earth and Planetary Interiors* 83: 197–216.
- Kuskov OL and Galimzyanov RF (1986) Thermodynamics of stable mineral assemblages of the mantle transition zone. In: Saxena SK (ed.) *Chemistry and Physics of the Terrestrial Planets*, pp. 310–361. New York: Springer-Verlag.
- Kuskov OL and Kronrod VA (1998) Constitution of the Moon: 5. Constraints on composition, density, temperature, and radius of a core. *Physics of the Earth and Planetary Interiors* 107: 285–306.
- Lahiri BN and Price AT (1939) Electromagnetic induction in non-uniform conductors, and the determination of the conductivity of the earth from terrestrial magnetic variations. *Philosophical Transactions of the Royal Society of London, Series A* 237: 509–540.
- Langevin Y (1997) The regolith of Mercury: Present knowledge and implications for the Mercury Orbiter mission. *Planetary and Space Sciences* 45: 31–37.
- Lay T, Heinz D, Ishil M, et al. (2005) Multidisciplinary impact of the deep mantle phase transition in perovskite structure. *EOS Transactions of the American Geophysical Union* 86: 1–5.
- Lee S, Zanolini M, Thode AM, Pappalardo RT, and Makris NC (2003) Probing Europa's interior with natural sound sources. *Icarus* 165: 144–167.
- Lemoine FG, Smith DE, Rowlands DD, et al. (2001) An improved solution of the gravity field of Mars (GMM-2B) from Mars Global Surveyor. *Journal of Geophysical Research* 106: 23359–23376.
- Lewis JS (1988) Origin and composition of Mercury. In: Vilas F, Chapman CR, and Matthews MS (eds.) *Mercury*, pp. 651–666. Tucson, AZ: University of Arizona Press.
- Liebermann RC (2005) The future of high-pressure mineral physics. *EOS Transactions of the American Geophysical Union* 86(40): 365–373.
- Lin RP, Mitchell DL, Curtis DW, et al. (1998) Lunar surface magnetic fields and their interaction with the solar wind: Results from Lunar Prospector. *Science* 281: 1480–1484.
- Lingenfelter RE and Schubert G (1973) Evidence for convection in planetary interiors from first-order topography. *Earth, Moon and Planets* 7: 172–180.
- Lognonné P (2005) Planetary seismology. *Annual Review of Earth and Planetary Sciences* 33: 571–604.
- Lognonné P and Mosser B (1993) Planetary seismology. *Survey in Geophysics* 14: 239–302.
- Lognonné P, Giardini D, and Banerdt B (2000) The NetLander very broad band seismometer. *Planetary and Space Sciences* 48: 1289–1302.
- Lognonné P, Gagnepain-Beyneix J, and Chenet H (2003) A new seismic model of the Moon: Implications for structure, thermal evolution and formation of the Moon. *Earth and Planetary Science Letters* 211: 27–44.
- Longhi J, Knittle E, Holloway JR, and Wänke H (1992) The bulk composition, mineralogy and internal structure of Mars. In: Kieffer HH, Jakosky BM, Snyder CW, and Matthews MS (eds.) *Mars*, pp. 184–208. Tucson, AZ: University of Arizona Press.

- Margot JL, Campbell DB, Jurgens RF, and Slade MA (1999) Topography of the lunar poles from radar interferometry: A survey of cold trap locations. *Science* 284: 1658–1660.
- McDonough WF and Sun S-S (1995) Composition of the Earth. *Chemical Geology* 120: 223–253.
- McKenzie D and Nimmo F (1997) Elastic thickness estimates for Venus from line of sight accelerations. *Icarus* 130: 198–216.
- McKenzie D, Ford PG, Johnson C, *et al.* (1992) Features on Venus generated by plate boundary processes. *Journal of Geophysical Research* 97(E8): 13533–13544.
- McKinnon WB, Zahnle KJ, Ivanov BA, and Melosh HJ (1997) Cratering on Venus: Models and observations. In: Bougher SW, Hunten DM, and Phillips RJ (eds.) *Venus II: Geology, Geophysics, Atmosphere, and Solar Wind Environment*, pp. 969–1014. Tucson, AZ: University of Arizona Press.
- McSween HY (1994) What we have learned about Mars from SNC meteorites. *Meteoritics* 29: 757–779.
- Meissner RO and Vetter UR (1979) Relationship between the seismic quality factor Q and the effective viscosity η^* . *Journal of Geophysics* 45: 147–158.
- Mizutani H (1995) Lunar interior exploration by Japanese lunar penetrator mission, Lunar-A. *Physics of the Earth* 43: 657–670.
- Moore WB and Schubert G (1997) Venusian crustal and lithospheric properties from nonlinear regressions of highland geoid and topography. *Icarus* 128: 415–428.
- Moore WB, Schubert G, Anderson JD, and Spencer JR (2006) The interior of Io. In: Lopes RMC and Spencer JR (eds.) *Io after Galileo*, pp. 89–108. Chichester, UK: Springer Verlag.
- Muhleman DO, Grossman AW, and Butler BJ (1995) Radar investigation of Mars, Mercury and Titan. *Annual Review of Earth and Planetary Sciences* 23: 337–374.
- Murakami M, Hirose K, Kawamura K, Sata N, and Ohishi Y (2004) Post-perovskite phase transition in MgSiO_3 . *Science* 304: 855–858.
- Nakamura Y (1983) Seismic velocity structure of the lunar mantle. *Journal of Geophysical Research* 88: 677–686.
- Nakamura Y (2005) Farside deep moonquakes and deep interior of the moon. *Journal of Geophysical Research* 110: E01001 (doi:10.1029/2004JE002332).
- Nakamura Y, Latham G, Lammlein D, Ewing M, Duennebie F, and Dorman J (1974) Deep lunar interior inferred from recent seismic data. *Geophysical Research Letters* 1: 137–140.
- Ness NF (1979) The magnetic fields of Mercury, Mars, and Moon. *Annual Review of Earth and Planetary Sciences* 7: 249–288.
- Neumann GA, Zuber MT, Smith DE, and Lemoine FG (1996) The lunar crust: Global structure and signature of major basins. *Journal of Geophysical Research* 101: 16841–16863.
- Neumann GA, Zuber MT, Wieczorek MA, McGovern PJ, Lemoine FG, and Smith DE (2004) Crustal structure of Mars from gravity and topography. *Journal of Geophysical Research* 109: E08002 (doi:10.1029/2004JE002262).
- Nimmo F and McKenzie D (1998) Volcanism and tectonics on Venus. *Annual Review of Earth and Planetary Sciences* 26: 23–51.
- Nimmo F and Stevenson DJ (2000) Influence of early plate tectonics on the thermal evolution and magnetic field of Mars. *Journal of Geophysical Research* 105: 11969–11979.
- Nimmo F and Stevenson DJ (2001) Estimates of Martian crustal thickness from viscous relaxation of topography. *Journal of Geophysical Research* 106: 5085–5098.
- Nimmo F and Tanaka K (2005) Early crustal evolution of Mars. *Annual Review of Earth and Planetary Sciences* 33: 133–161.
- Nozette S, Rustan P, Pleasance LP, *et al.* (1994) The Clementine mission to the Moon: Scientific overview. *Science* 266: 1835–1839.
- Oganov AR and Ono S (2004) Theoretical and experimental evidence for a post-perovskite phase of MgSiO_3 perovskite in Earth's D" layer. *Nature* 430: 445–448.
- Olsen N (1999) Induction studies with satellite data. *Survey in Geophysics* 20: 309–340.
- Peale SJ (1976) Inferences from the dynamical history of Mercury's rotation. *Icarus* 28: 459–467.
- Peale SJ (1988) The rotational dynamics of Mercury and the state of its core. In: Vilas F, Chapman CR, and Matthews MS (eds.) *Mercury*, pp. 461–493. Tucson, AZ: University of Arizona Press.
- Phillips JL and Russell CT (1987) Upper limit on the intrinsic magnetic field of Venus. *Journal of Geophysical Research* 92(A3): 2253–2263.
- Phillips RJ (1994) Estimating lithospheric properties at Atla Regio, Venus. *Icarus* 112: 147–170.
- Pieters CM and Tompkins S (1999) Tsiolkovsky crater: A window into crustal processes on the lunar farside. *Journal of Geophysical Research* 104: 21935–21950.
- Pieters CM, Tompkins S, Head JW, and Hess PC (1997) Mineralogy of the mafic anomaly in the South Pole-Aitken basin: Implications for excavation of the lunar mantle. *Geophysical Research Letters* 24: 1903–1906.
- Platzman GW (1984) Planetary energy balance for tidal dissipation. *Reviews in Geophysics and Space Physics* 22: 73–84.
- Poirier JP and Liebermann RC (1984) On the activation volume for creep and its variation with depth in the Earth's lower mantle. *Physics of the Earth and Planetary Interiors* 35: 283–293.
- Porco CC, Helfenstein P, Thomas PC, *et al.* (2006) Cassini observes the active South Pole of Enceladus. *Science* 311: 1393–1401.
- Press WH, Flannery BP, Teukolsky SA, and Vetterling WT (1992) *Numerical Recipes*. New York: Cambridge University Press.
- Ranalli G (1987) *Rheology of the Earth. Deformation and Flow Processes in Geophysics and Geodynamics*. Winchester, MA: Allen & Unwin.
- Rappaport NJ, Konopliv AS, Kucinskis AB, and Ford PG (1999) An improved 360 degree and order model of Venus topography. *Icarus* 139: 19–31.
- Righter K and Drake MJ (1996) Core formation in Earth's moon, Mars, and Vesta. *Icarus* 124: 513–529.
- Righter K and Drake MJ (1997) A magma ocean on Vesta: Core formation and petrogenesis of eucrites and diogenites. *Meteorites and Planetary Science* 32: 929–944.
- Rikitake T (1966) *Electromagnetism and the Earth's Interior*. Amsterdam. The Netherlands: Elsevier.
- Ringwood AE (1975) *Composition and Petrology of the Earth's Mantle*. New York: McGraw-Hill.
- Roberts JH and Zhong S (2006) Degree-1 convection in the Martian mantle and the origin of the hemispheric dichotomy. *Journal of Geophysical Research* 111: E06013 (doi:10.1029/2005JE002668).
- Roberts RG (1986) Global electromagnetic induction. *Survey in Geophysics* 8: 339–374.
- Russell CT (1980) Planetary magnetism. *Reviews of Geophysics* 18: 77–106.
- Russell CT, Coleman PJ, Jr., Fleming BK, *et al.* (1975) The fine-scale lunar magnetic field. *Proceedings of the 6th Lunar and Science Conference*, Vol. 3, pp. 2955–2969. The MIT Press.
- Russell CT, Coleman PJ, Jr., Lichtenstein BR, Schubert G, and Sharp LR (1973) Subsatellite measurements of the lunar magnetic field. *Proceedings of the 4th Lunar and Science Conference*, Vol. 3, pp. 2833–2845. The MIT Press.
- Sandwell DT and Schubert G (1992a) Evidence for retrograde lithospheric subduction on Venus. *Science* 257: 766–770.
- Sandwell DT and Schubert G (1992b) Flexural ridges, trenches, and outer rises around coronae on Venus. *Journal of Geophysical Research* 97(E10): 16069–16083.

- Sanloup C, Jambon A, and Gillet P (1999) A simple chondritic model of Mars. *Physics of the Earth and Planetary Interiors* 112: 43–54.
- Sanloup C, Guyot F, Gillet P, Fiquet G, Mezouar M, and Martinez I (2000) Density measurements of liquid Fe-S alloys at high-pressure. *Geophysical Research Letters* 27: 811–814.
- Schaber GG, Strom RG, Moore HJ, *et al.* (1992) Geology and distribution of impact craters on Venus - what are they telling us. *Journal of Geophysical Research* 97(E8): 13257–13301.
- Schubert G, Anderson JD, Spohn T, and McKinnon WB (2004) Interior composition, structure and dynamics of the Galilean satellites. In: Bagenal F, Dowling TE, and McKinnon WB (eds.) *Jupiter: The planet, satellites and magnetosphere*, pp. 281–306. Cambridge, UK: Cambridge University Press.
- Schubert G, Anderson JD, Travis BJ, and Palguta J (in press) Enceladus: Present internal structure and differentiation by early and long term radiogenic heating. *Icarus*.
- Schubert G and Lingenfelter RE (1973) Martian centre of mass – Centre of figure offset. *Nature* 242: 251–252.
- Schubert G and Schwartz K (1969) A theory for the interpretation of lunar surface magnetometer data. *The Moon* 1: 106–117.
- Schubert G and Spohn T (1990) Thermal history of Mars and the sulfur content of its core. *Journal of Geophysical Research* 95: 14095–14104.
- Schubert G, Ross MN, Stevenson DJ, and Spohn T (1988) Mercury's thermal history and the generation of its magnetic field. In: Vilas F, Chapman CR, and Matthews MS (eds.) *Mercury*, pp. 429–460. Tucson, AZ: University of Arizona Press.
- Schubert G, Solomon SC, Turcotte DL, Drake MJ, and Sleep NH (1992) Origin and thermal evolution of Mars. In: Kieffer HH, Jakosky BM, Snyder CW, and Matthews MS (eds.) *Mars*, pp. 147–183. Tucson, AZ: University of Arizona Press.
- Schubert G, Zhang K, Kivelson MG, and Anderson JD (1996) The magnetic field and internal structure of Ganymede. *Nature* 384: 544–545.
- Schubert G, Solomatov VS, Tackley PJ, and Turcotte DL (1997) Mantle convection and the thermal evolution of Venus. In: Bougher SW, Hunten DM, and Philips RJ (eds.) *Venus II: Geology, Geophysics, Atmosphere, and Solar Wind Environment*, pp. 1245–1287. Tucson, AZ: University of Arizona Press.
- Schubert G, Russell CT, and Moore WB (2000) Timing of the Martian dynamo. *Nature* 408: 666–667.
- Schubert G, Turcotte DL, and Olson P (2001) *Mantle Convection in the Earth and Planets*. Cambridge, UK: Cambridge University Press.
- Schuster A (1889) The diurnal variation of terrestrial magnetism. *Philosophical Transactions of the Royal Society of London Series A* 180: 467–518.
- Seidelmann PK, Abalkin VK, Bursa M, *et al.* (2002) Report of the IAU/IAG working group on cartographic coordinates and rotational elements of the planets and satellites: 2000. *Celestial Mechanics and Dynamical Astronomy* 82: 83–110.
- Seiff A (1983) Thermal structure of the atmosphere of Venus. In: Hunten DM, Colin L, Donahue TM, and Moroz VI (eds.) *Venus*, pp. 154–158. Tucson, AZ: University of Arizona Press.
- Sellers PC (1992) Seismic evidence for a low-velocity lunar core. *Journal of Geophysical Research* 97: 11663–11672.
- Senske DA, Schaber GG, and Stofan ER (1992) Regional topographic rises on Venus – Geology of Western Eistla Regio and comparison to Beta Regio and Atla Regio. *Journal of Geophysical Research* 97(E8): 13395–13420.
- Shampine LF and Gordon MK (1975) *Computer Solution of Ordinary Differential Equations. The Initial Value Problem*. San Francisco, CA: Freeman.
- Shearer CK, Hess PC, Wiecek MA, *et al.* (2006) Thermal and magmatic evolution of the Moon. *Reviews in Mineralogy and Geochemistry* 60: 365–518.
- Siegfried RW and Solomon SC (1974) Mercury: Internal structure and thermal evolution. *Icarus* 23: 192–205.
- Simons M, Hager BH, and Solomon SC (1994) Global variations in the geoid/topography admittance of Venus. *Science* 264: 798–803.
- Sjogren WL, Banerdt WB, Chodas PW, *et al.* (1997) The Venus gravity field and other geodetic parameters. In: Bougher SW, Hunten DM, and Philips RJ (eds.) *Venus II: Geology, Geophysics, Atmosphere, and Solar Wind Environment*, pp. 1125–1162. Tucson, AZ: University of Arizona Press.
- Sloan ED (2003) Fundamental principles and applications of natural gas hydrates. *Nature* 426: 353–359.
- Smith DE and Zuber MT (1996) The shape of Mars and the topographic signature of the hemispheric dichotomy. *Science* 271: 184–187.
- Smith DE, Zuber MT, and Solomon SC (1999a) The global topography of Mars and implications for surface evolution. *Science* 284: 1495–1503.
- Smith DE, Sjogren WL, Tyler GL, Balmino G, Lemoine FG, and Konopliv AS (1999b) The gravity field of Mars: Results from Mars Global Surveyor. *Science* 286: 94–97.
- Smith JC and Born GH (1976) Secular acceleration of Phobos and Q of Mars. *Icarus* 27: 51–53.
- Smith JV, Anderson AT, Newton RC, *et al.* (1970) Petrologic history of the Moon inferred from petrography, mineralogy, and petrogenesis of Apollo 11 rocks. *Proceedings of the Apollo 11 Lunar and Science Conference*, Vol. 1, pp. 897–925. Pergamon Press.
- Smrekar SE (1994) Evidence for active hotspots on Venus from analysis of Magellan gravity data. *Icarus* 112: 2–26.
- Sohl F and Spohn T (1997) The interior structure of Mars: Implications from SNC meteorites. *Journal of Geophysical Research* 102: 1613–1635.
- Sohl F, Hussmann H, Schwentker B, Spohn T, and Lorenz RD (2003) Interior structure models and tidal Love numbers of Titan. *Journal of Geophysical Research* 108(E12): 5130 (doi:10.1029/2003JE002044).
- Sohl F, Schubert G, and Spohn T (2005) Geophysical constraints on the composition and structure of the Martian interior. *Journal of Geophysical Research* 110: E12008 (doi:10.1029/2005JE002520).
- Solomon SC (2003) Mercury: The enigmatic innermost planet. *Earth and Planetary Science Letters* 216: 441–455.
- Solomon SC, Aharonson O, Aurnou JM, *et al.* (2005) New perspectives on ancient Mars. *Science* 307: 1214–1220.
- Sonett CP (1982) Electromagnetic induction in the moon. *Reviews in Geophysics and Space Physics* 20: 411–455.
- Sonett CP, Colburn DS, Dyal P, *et al.* (1971) Lunar electrical conductivity profile. *Nature* 230: 359–362.
- Sonett CP, Smith BF, Colburn DS, Schubert G, and Schwartz K (1972) The induced magnetic field of the Moon: Conductivity profiles and inferred temperatures. *Proceedings of the 3rd Lunar and Science Conference, Geochimica et Cosmochimica Acta, Supplement 3*, pp. 2309–2336. The MIT Press.
- Spencer JR, Pearl JC, Segura M, *et al.* (2006) Cassini encounters Enceladus: Background and the discovery of a south polar hot spot. *Science* 311: 1401–1405.
- Spohn T (1991) Mantle differentiation and thermal evolution of Mars, Mercury, and Venus. *Icarus* 90: 222–236.
- Spohn T, Sohl F, and Breuer D (1998) Mars. *Astronomical and Astrophysical Review* 8: 181–235.

- Spohn T, Acuña MH, Breuer D, *et al.* (2001a) Geophysical constraints on the evolution of Mars. *Space Science Review* 96: 231–262.
- Spohn T, Sohl F, Wiczerkowski K, and Conzelmann V (2001b) The interior structure of Mercury: What we know, what we expect from BepiColombo. *Planetary and Space Sciences* 49: 1561–1570.
- Sprague AL, Kozłowski RWH, Witteborn FC, Cruikshank DP, and Wooden DH (1994) Mercury: Evidence for anorthosite and basalt from mid-infrared (7.3–13.5 μm) spectroscopy. *Icarus* 109: 156–167.
- Stacey FD (1977) Applications of thermodynamics to fundamental Earth physics. *Geophysical Survey* 3: 175–204.
- Stacey FD, Brennan BJ, and Irvine RD (1981) Finite strain theories and comparisons with seismological data. *Geophysical Survey* 4: 189–232.
- Stevenson DJ, Spohn T, and Schubert G (1983) Magnetism and thermal evolution of the terrestrial planets. *Icarus* 54: 466–489.
- Stofan ER, Hamilton VE, Janes DM, and Smrekar SE (1997) Coronae on Venus: Morphology and origin. In: Bougher SW, Hunten DM, and Philips RJ (eds.) *Venus II: Geology, Geophysics, Atmosphere, and Solar Wind Environment*, pp. 931–965. Tucson, AZ: University of Arizona Press.
- Strom RG (1987) *Mercury: The Elusive Planet*. Washington, D.C.: Smithsonian Institution Press.
- Strom RG (1997) Mercury: An overview. *Advances in Space Research* 19: 1471–1485.
- Surkov YA (1983) Studies of Venus rocks by Veneras 8, 9, and 10. In: Hunten DM, Colin L, Donahue TM, and Moroz VI (eds.) *Venus*, pp. 154–158. Tucson, AZ: University of Arizona Press.
- Tarits P (1994) Electromagnetic studies of global geodynamic processes. *Survey in Geophysics* 15: 209–238.
- Tobie G, Grasset O, Lunine JI, Mocquet A, and Sotin C (2005) Titan's internal structure inferred from a coupled thermal-orbital model. *Icarus* 175: 496–502.
- Toksöz MN, Dainty AM, Solomon SC, and Anderson KR (1974) Structure of the Moon. *Reviews of Geophysics* 12: 539–567.
- Tsuchiya T, Tsuchiya J, Umemoto K, and Wentzcovitch RM (2004) Phase transition in MgSiO_3 perovskite in the earth's lower mantle. *Earth and Planetary Science Letters* 224: 241–248.
- Turcotte DL (1993) An episodic hypothesis for Venusian tectonics. *Journal of Geophysical Research* 98(E9): 17061–17068.
- Valencia D, O'Connell RJ, and Sasselov DD (2006) Internal structure of massive terrestrial planets. *Icarus* 181: 545–554.
- Valencia D, Sasselov DD, and O'Connell RJ (2007) Radius and structure of the first super-earth planet. *Astrophysical Journal* 656: 545–551.
- Van Hemelrijck E and Vercheval J (1981) Some aspects of the solar radiation incident at the top of the atmospheres of Mercury and Venus. *Icarus* 48: 167–179.
- Van Hoolst T and Jacobs C (2003) Mercury's tides and interior structure. *Journal of Geophysical Research* 108(E11): 5121 (doi:10.1029/2003JE002126).
- Van Hoolst T, Dehant V, Roosbeek F, and Lognonné P (2003) Tidally induced surface displacements, external potential variations, and gravity variations on Mars. *Icarus* 161: 281–296.
- van Thienen P, Rivoldini A, Van Hoolst T, and Lognonné P (2006) A top-down origin for martian mantle plumes. *Icarus* 185: 197–210.
- Vasavada AR, Paige DA, and Wood SE (1999) Near-surface temperatures on Mercury and the Moon and the stability of polar ice deposits. *Icarus* 141: 179–193.
- Verhoeven O, Rivoldini A, Vacher P, *et al.* (2005) Interior structure of terrestrial planets: Modelling Mars' mantle and its electromagnetic, geodetic and seismic properties. *Journal of Geophysical Research* 110: E04009 (doi:10.1029/2004JE002271).
- Vilas F (1985) Mercury: Absence of crystalline Fe^{2+} in the regolith. *Icarus* 64: 133–138.
- Voorhies CV, Sabaka TJ, and Purucker M (2002) On magnetic spectra of Earth and Mars. *Journal of Geophysical Research* 107(E6): 5034 (doi:10.1029/2001JE001534).
- Wänke H and Dreibus G (1988) Chemical composition and accretion history of terrestrial planets. *Philosophical Transactions of the Royal Society of London Series A* 325: 545–557.
- Warell J and Blewett DT (2004) Properties of the Hermean regolith. V. New optical reflectance spectra, comparison with lunar anorthosites, and mineralogical modelling. *Icarus* 168: 257–276.
- Warren PH (1985) The magma ocean concept and lunar evolution. *Annual Review of Earth and Planetary Sciences* 13: 201–240.
- Wasson JT (1988) The building stones of Mercury. In: Vilas F, Chapman CR, and Matthews MS (eds.) *Mercury*, pp. 692–708. Tucson, AZ: University of Arizona Press.
- Watt JP, Davies GF, and O'Connell RJ (1976) The elastic properties of composite materials. *Reviews of Geophysics* 14: 541–563.
- Watters TR and McGovern PJ (2005) Hemispheres apart: The martian crustal dichotomy. *EOS Transactions of the American Geophysical Union* 86(5): 46–47.
- Weitz CM and Basilevsky AT (1993) Magellan observations of the Venera and Vega landing site regions. *Journal of Geophysical Research* 98(E9): 17069–17097.
- Wessel P and Smith WHF (1991) Free software helps map and display data. *EOS Transactions of the American Geophysical Union* 72: 441; 445–446.
- Wieczorek MA and Phillips RJ (1998) Potential anomalies on a sphere: Applications to the thickness of the lunar crust. *Journal of Geophysical Research* 103: 1715–1724.
- Wieczorek MA and Phillips RJ (1999) Lunar multiring basins and the cratering process. *Icarus* 139: 246–259.
- Wieczorek MA and Phillips RJ (2000) The Procellarum KREEP Terrane: Implications for mare volcanism and lunar evolution. *Journal of Geophysical Research* 105: 20417–20430.
- Wieczorek MA and Zuber MT (2001) The composition and origin of the lunar crust: Constraints from central peaks and crustal thickness modeling. *Geophysical Research Letters* 28: 4023–4026.
- Wieczorek MA and Zuber MT (2004) Thickness of the martian crust: Improved constraints from geoid-to-topography ratios. *Journal of Geophysical Research* 109: E01009 (doi:10.1029/2003JE002153).
- Wieczorek MA, Zuber MT, and Phillips RJ (2001) The role of magma buoyancy on the eruption of lunar basalts. *Earth and Planetary Science Letters* 185: 71–83.
- Wieczorek MA, Jolliff BL, Khan A, *et al.* (2006) The constitution and structure of the lunar interior. *Reviews in Mineralogy and Geochemistry* 60: 221–364.
- Wilhelms DE (1976) Mercurian volcanism questioned. *Icarus* 28: 551–558.
- Wilhelms DE and Squyres SW (1984) The Martian hemispheric dichotomy may be due to a giant impact. *Nature* 309: 138–140.
- Williams JG, Boggs DH, Yoder CF, Ratcliff JT, and Dickey JO (2001) Lunar rotational dissipation in solid body and molten core. *Journal of Geophysical Research* 106: 27933–27968.
- Wood BJ (1993) Carbon in the core. *Earth and Planetary Science Letters* 117: 593–607.

- Wood JA, Dickey JS, Marvin UB, and Powell BN (1970) Lunar anorthosites and a geophysical model of the Moon. *Proceedings of the Apollo 11 Lunar and Science Conference*, Vol. 1, pp. 965–988 Pergamon Press.
- Wood JA, Anderson DL, Buck WR, *et al.* (1981) Geophysical and cosmochemical constraints on properties of mantles of the terrestrial planets. In: Kaula WM (ed.) *Basaltic Volcanism on the Terrestrial Planets*, pp. 633–699. New York: Pergamon.
- Yoder CF (1981) The free librations of a dissipative Moon. *Philosophical Transactions of the Royal Society of London Series A* 303: 327–338.
- Yoder CF (1982) Tidal rigidity of Phobos. *Icarus* 49: 327–346.
- Yoder CF (1997) Venusian spin dynamics. In: Bougher SW, Hunten DM, and Phillips RJ (eds.) *Venus II: Geology, Geophysics, Atmosphere, and Solar Wind Environment*, pp. 1087–1124. Tucson, AZ: University of Arizona Press.
- Yoder CF and Standish EM (1997) Measurements of the precession and rotation from Viking lander range data. *Journal of Geophysical Research* 102: 4065–4080.
- Yoder CF, Konopliv AS, Yuan DN, Standish EM, and Folkner WM (2003) Fluid core size of Mars from detection of the solar tide. *Science* 300: 299–303.
- Zhong S and Zuber MT (2001) Degree-1 mantle convection and the crustal dichotomy of Mars. *Earth and Planetary Science Letters* 189: 75–84.
- Zimmer C, Khurana KK, and Kivelson MG (2000) Subsurface oceans on Europa and Callisto: Constraints from Galileo magnetometer observations. *Icarus* 147: 329–347.
- Zuber MT (2001) The crust and mantle of Mars. *Nature* 412: 220–227.
- Zuber MT, Smith DE, Lemoine FG, and Neumann GA (1994) The shape and internal structure of the Moon from the Clementine mission. *Science* 266: 1839–1843.
- Zuber MT, Smith DE, Solomon SC, *et al.* (1992) The Mars Observer laser altimeter investigation. *Journal of Geophysical Research* 97: 7781–7797.
- Zuber MT, Solomon SC, Phillips RJ, *et al.* (2000) Internal structure and early thermal evolution of Mars from Mars Global Surveyor topography and gravity. *Science* 287: 1788–1793.